PCCP

High-Fidelity First Principles Nonadiabaticity: Diabatization, Analytic Representation of Global Diabatic Potential Energy Matrices, and Quantum Dynamics

Journal:	*Physical Chemistry Chemical Physics*
Manuscript ID	CP-PER-07-2021-003008.R1
Article Type:	Perspective
Date Submitted by the Author:	31-Jul-2021
Complete List of Authors:	Guan, Yafu; Johns Hopkins University, Xie, Changjian; Northwest University, Institute of Modern Physics Yarkony, David; Johns Hopkins University, Department of Chemistry Guo, Hua; University of New Mexico College of Arts and Sciences, Department of Chemistry and Chemical Biology

Submitted to PCCP, 7/1/2021, revised 7/30/2021

High-Fidelity First Principles Nonadiabaticity: Diabatization, Analytic Representation of Global Diabatic Potential Energy Matrices, and Quantum Dynamics

Yafu Guan,[1,*] Changjian Xie,[2,*] David R. Yarkony[1, *] and Hua Guo,[3, *]

[1]*Department of Chemistry, Johns Hopkins University, Baltimore, Maryland 21218, USA*

[2]*Institute of Modern Physics, Northwest University, Xi'an, Shaanxi 710069, China*

[3]*Department of Chemistry and Chemical Biology, University of New Mexico, Albuquerque, New Mexico, 87131, USA*

*: corresponding authors: yguan15@jhu.edu, chjxie@nwu.edu.cn, hguo@unm.edu, yarkony@jhu.edu

Abstract

Nonadiabatic dynamics, which goes beyond the Born-Oppenheimer approximation, has increasingly been shown to play an important role in chemical processes, particularly those involving electronically excited states. Understanding multistate dynamics requires rigorous quantum characterization of both electronic and nuclear motion. However, such first principles treatments of multi-dimensional systems have so far been rather limited due to the lack of accurate coupled potential energy surfaces and difficulties associated with quantum dynamics. In this Perspective, we review recent advances in developing high-fidelity analytical diabatic potential energy matrices for quantum dynamical investigations of polyatomic uni- and bi-molecular nonadiabatic processes, by machine learning of high-level *ab initio* data. Special attention is paid to methods of diabatization, high fidelity construction of multi-state coupled potential energy surfaces and property surfaces, as well as quantum mechanical characterization of nonadiabatic nuclear dynamics. To illustrate the tremendous progress made by these new developments, several examples are discussed, in which direct comparison with quantum state resolved measurements led to either confirmation of the observation or sometimes reinterpretation of the experimental data. The insights gained in these prototypical systems greatly advance our understanding of nonadiabatic dynamics in chemical systems.

1. Introduction

Our understanding of chemical processes is largely based on the adiabatic paradigm proposed by Born and Oppenheimer (BO),[1] in which the motion of the electrons is separated from that of the nuclei. Such a separation is justified in general, given the mass disparity between the two types of particles. Computationally, this separation of motion formed the foundation for modern electronic structure theory,[2] in which the electronic Schrödinger equation is solved at fixed nuclear geometries. This adiabatic representation also gave birth to the concept of the potential energy surface (PES),[3] which is a multidimensional hypersurface of the electronic energy (plus nuclear repulsion) as a function of molecular geometry. Under thermal conditions, most systems can indeed be considered on the ground state PES, which governs the nuclear dynamics leading to spectroscopy and reactivity. Recent advances in constructing PESs for prototypical systems have led to unprecedented insights into adiabatic reaction dynamics.[4-6]

Despite the success of the BO approximation, there is increasing evidence that more than one adiabatic state might be involved in many chemical processes, particularly those involving excited state species.[7-16] In photochemical processes, for example, the excited electronic state prepared by photoexcitation might undergo transitions to other electronic states through couplings near an actual or avoided crossing between two or more PESs.[17-23] Bimolecular collisions can also be strongly influenced by nonadiabatic transitions.[11, 12, 24] These features are due to electronic degeneracies, some accidental and others required by symmetry,[25, 26] and have been noted from the dawn of quantum mechanics.[27-30] A commonly encountered type of degeneracy between states with the same total electron spin is a conical intersection (CI), which consists of an N-2 dimensional crossing seam where N is the dimensionality of system.[31] The degeneracy between cone-shaped upper and lower adiabats facilitates facile nonadiabatic transitions taking place

between the states in the vicinity of the CI. Such crossings have profound impact on nuclear dynamics, because they often serve as the funnel for population transfer from the upper to lower electronic states in what is called internal conversion (IC).[8] For processes ostensibly occurring on the ground state PES, coupling with one or more excited states may still have a significant impact, even when the energy is significantly lower than that of the crossing point. A good example is the geometric phase (GP) effect around a CI,[24, 32-34] which can generate a strong interference between pathways around the CI seam in the adiabatic representation. Another class of nonadiabatic effects is due to spin-orbit coupling (SOC), which facilitates intersystem crossing (ISC) between states with different spin multiplicities.[14] IC and ISC are two major mechanisms for non-radiative decay of excited state molecules, and they may coexist in the same system. Yet, their competition in nonadiabatic dynamics has seldom investigated quantum mechanically on an equal footing, with few exceptions.[35]

It is clear that a better understanding of these nonadiabatic processes requires the inclusion of more than one electronic state in a full quantum treatment. Given the non-local nature of quantum mechanics, a rigorous treatment of the nuclear dynamics demands knowledge of the global PESs and their couplings. This is in principle still possible in the adiabatic representation, in which the couplings ignored in the BO limit can be included in the Hamiltonian.[36, 37] However, this approach is numerically inconvenient because adiabatic PESs are not smooth at the crossing seam, making an analytic single-surface representation impossible. Moreover, the nonadiabatic coupling operator is singular in the adiabatic representation at the CI seam, leading to numerical instability in nuclear dynamics.[36, 38] As discussed in Section II, it is far more advantageous to work within a quasi-diabatic representation, in which the singular operators are removed and coupled PESs are given as a diabatic potential energy matrix (DPEM), the elements of which are smooth

functions of the nuclear coordinates.[36, 39, 40] However, diabatization and the construction of these DPEMs are challenging, particularly in a multi-dimensional configuration space.[41] First, an exact diabatization for polyatomic systems is impracticable because it requires information on all the electronic states,[42, 43] as discussed below. As a result, only approximate diabatization is possible, thus the prefix "quasi". (For simplicity, this qualifier will be dropped in the remainder of this Perspective, but one needs to keep in mind that the diabatic representation is not unique.) Second, because electronic structure calculations are necessarily performed in the adiabatic representation, there is a need to transform the results to a diabatic representation and this transformation is dependent on the nuclear coordinates. There are many ways to perform such diabatization, with different advantages and disadvantages. Third, a faithful representation is required to provide an accurate account of all electronic structure information in high dimensionality for polyatomic systems. For these reasons, rigorous first principles characterization of nonadiabatic dynamics has until recently been restricted to few small systems with only qualitative accuracy.

There is significant interest in studying nonadiabatic dynamics using direct dynamics approaches, in which the forces and nonadiabatic couplings are computed on the fly.[44-48] These approaches are ideal for exploring various reaction channels and provide useful information about nonadiabatic dynamics. However, numerical costs associated with these on-the-fly approaches are often overwhelming so that the electronic structure is not treated with the highest possible level of theory. We note in particular that on-the-fly dynamics based on time-dependent density functional theory, which is the work horse in many excited state studies, often fails to describe the CI seams.[49-51] In addition, the treatment of nuclear motion is often approximated with a restrictive basis set, such as a Gaussian wave packet,[44, 45] or with classical trajectories.[46, 47] For these reasons, the results

may not be quantitative accurate, particularly for long time events and for quantum state resolved observables.

To gain quantitatively accurate insights into nonadiabatic dynamics, it is desirable to study systems that a first-principles treatment of both the electronic and nuclear degrees of freedom (DOFs) is possible, especially when experimental data are available. A complete understanding of these prototypical processes is beneficial for similar systems of larger sizes and serves as benchmark for developing more approximate methods and models. Recently, much progress has been made in developing accurate global multidimensional DPEMs based on high-level *ab initio* calculations for several such important molecular systems. These advances significantly improved our ability to investigate nonadiabatic dynamics in polyatomic systems using rigorous quantum mechanical (and semi-classical) methods, which is important as molecular systems are intrinsically quantum and need be treated as such.[41] Since these chosen systems have been extensively studied by experimentalists, some with quantum state resolution, our approach enabled a direct comparison with measurements in exquisite detail. Thanks to the high accuracy of the DPEMs and the rigorous quantum mechanical treatment of nuclear dynamics, excellent agreement with experimental observations is often achievable. In some cases, details provided by the first-principles approach have challenged earlier models and in some cases offered reinterpretations of experimental data, thus advancing our understanding of these complex phenomena. Since the review of this field by two of the current authors in 2016,[41] there has been tremendous progress in this direction. In this Perspective, we survey these advances and discuss how the progress has impacted our knowledge of nonadiabatic processes. This manuscript is organized as follows. The adiabatic and diabatic representations and their transformation are discussed in Sec. 2, while various diabatization schemes are reviewed in Sec. 3. Detailed discussion is given in Sec. 4 on the

construction of DPEMs and in Sec. 5 on quantum dynamics. Several prototypical examples are discussed in Sec. 6, particularly on their comparison with experiment. Finally, a summary and prospects are given in the last section (Sec. 7).

2. Adiabatic and Diabatic Representations

2.1. Adiabatic States and the Born-Oppenheimer Approximation

The total wave function, $\Psi_\kappa^T(\mathbf{r},\mathbf{R})$, satisfies the electronic-nuclear Schrödinger equation:

$$(\hat{H}^T - E_\kappa)\Psi_\kappa^T(\mathbf{r},\mathbf{R}) = 0\,, \tag{2.1a}$$

where the total Hamiltonian is given by:

$$\hat{H}^T = \hat{T}_N + \hat{H}^e(\mathbf{r};\mathbf{R}) \quad \text{where} \qquad \hat{T}_N = -\frac{1}{2}\sum_{\alpha=1}^{3N^n}\frac{1}{m_\alpha}\frac{\partial^2}{\partial R_\alpha^2}\,. \tag{2.1b}$$

Here, $\hat{H}^e$ is the electronic Hamiltonian in the Coulomb approximation, which parametrically (indicated by a semi-colon, ;) depends on nuclear coordinates, $\hat{T}_N$ is the nuclear kinetic energy operator, with **r** being $3N^e$ electronic coordinates and, unless otherwise noted, **R** are $3N^n$ nuclei centered Cartesian coordinates. Throughout this work, vectors and matrices will be written in bold face while their scalar components are in italics.

$\Psi_\kappa^T(\mathbf{r},\mathbf{R})$ is expanded in a geometry dependent basis (adaptive griding) of electronic wave functions $\psi_J^{(e)}$ (J = 1, 2, … , N^{state}) for either the adiabatic $e = a$ or diabatic for $e = d$ representation:

$$\Psi_\kappa^T(\mathbf{r},\mathbf{R}) = \sum_J^{N^{state}} \psi_J^{(e)}(\mathbf{r};\mathbf{R})\chi_J^{(e),\kappa}(\mathbf{R})\,. \tag{2.2}$$

Thus, each term in Eq. (2.2) is a product of a nuclear wave function, a function only of **R** and an electronic wave function, a function of **r** and depending parametrically on **R**. The adiabatic (basis) wave functions satisfy the electronic Schrödinger equation:

$$\left[\mathbf{H}^{e}-\mathbf{E}^{(a),J,(ab)}\right]\psi_{J}^{(a)}=0\ . \tag{2.3}$$

The electronic space in Eq. (2.3) is spanned by a basis of dimension N^M. Here, $N^M = N^{ab}$ where *ab* stands for *ab initio.* In practice, only the first N^{state} eigenstates are used.

In the adiabatic representation and assuming $\boldsymbol{\psi}^{(a)}(\mathbf{r};\mathbf{R})$ is real-valued (which has its limitations - see below), Eq. (2.1) becomes

$$\left\{\sum_{\alpha=1}^{3N^n}\frac{-1}{m_\alpha}\left[\frac{\partial^2}{\partial R_\alpha^2}\mathbf{I}+2\mathbf{f}_\alpha^{(a)}\frac{\partial}{\partial R_\alpha}+\mathbf{B}_{\alpha\alpha}^{(a)}\right]-E_\kappa\mathbf{I}+\mathbf{E}^{(a),(ab)}(\mathbf{R})\right\}\boldsymbol{\chi}^{(a),\kappa}=0\,, \tag{2.4a}$$

$$[\sum_{\alpha=1}^{3N^n}\frac{-1}{2m_\alpha}[\frac{\partial}{\partial R_\alpha}\mathbf{I}+i\mathbf{f}^{(a)}]^2-E_\kappa\mathbf{I}+\mathbf{E}^{(a),(ab)}(\mathbf{R})]\boldsymbol{\chi}^{(a),\kappa}=0\,, \tag{2.4b}$$

where **I** is an $N^{state}\times N^{state}$ unit matrix. The derivative coupling matrix elements are defined as

$$f_\alpha^{(a),I,J}(\mathbf{R})=\left\langle\psi_I^{(a)}(\mathbf{r};\mathbf{R})\left|\frac{\partial}{\partial R_\alpha}\psi_J^{(a)}(\mathbf{r};\mathbf{R})\right.\right\rangle_{\mathbf{r}}\,, \tag{2.5a}$$

the second derivative coupling matrix elements as

$$B_{\alpha\alpha}^{(a),I,J}(\mathbf{R})=\left\langle\psi_I^{(a)}(\mathbf{r};\mathbf{R})\left|\frac{\partial^2}{\partial R_\alpha^2}\psi_J^{(a)}(\mathbf{r};\mathbf{R})\right.\right\rangle_{\mathbf{r}}\,, \tag{2.5b}$$

and derived Eq. (2.4b) from Eq. (2.4a) using

$$\frac{\partial}{\partial R_\alpha} f_\alpha^{(a),I,J} + \sum_{K=1}^{N^{ab}} f_\alpha^{(a),K,I} f_\alpha^{(a),K,J} = B_{\alpha\alpha}^{(a),I,J}, \tag{2.5c}$$

which assumes the electronic basis is complete. We emphasize that **f** and **B** are vectors in the nuclear coordinates and matrices in the electronic state labels. The diagonal terms of the $B_{\alpha\alpha}^{(a),I,I}$ matrix are referred to as the Diagonal Born-Oppenheimer corrections (DBOC). **f** and **B** are singular at a CI. When $N^{state} = 1$ and neglecting its DBOC, we recover the standard BO approximation.

2.2. Diabatic Representation and Adiabatic-to-Diabatic Transformation

The diabatic representation is formally a unitary transformation **U**(**R**) of the adiabatic representation

$$\boldsymbol{\psi}^{(d)} = \mathbf{U}\boldsymbol{\psi}^{(a)}, \tag{2.6a}$$

where **U** is the unitary adiabatic-to-diabatic (AtD) transformation. So from Eq. (2.2), we have

$$\boldsymbol{\chi}^{(d)} = \mathbf{U}^\dagger \boldsymbol{\chi}^{(a)}. \tag{2.6b}$$

In the diabatic representation, the derivative coupling vanishes,[39, 43, 52] that is

$$\begin{aligned} f_\alpha^{(d),I,J}(\mathbf{R}) &= \left\langle \psi_I^{(d)}(\mathbf{r};\mathbf{R}) \middle| \frac{\partial}{\partial R_\alpha} \psi_J^{(d)}(\mathbf{r};\mathbf{R}) \right\rangle \\ &= \left\langle \sum_K U_{I,K} \psi_K^{(a)}(\mathbf{r};\mathbf{R}) \middle| \frac{\partial}{\partial R_\alpha} \sum_L U_{J,L} \psi_L^{(a)}(\mathbf{r};\mathbf{R}) \right\rangle \\ &= \sum_{K,L} \left\langle U_{I,K}\psi_K^{(a)} \,|\, (U_{J,L}) \frac{\partial}{\partial R_\alpha} \psi_L^{(a)} + U_{I,K}\psi_K^{(a)} \middle| (\frac{\partial}{\partial R_\alpha} U_{J,L}) \psi_L^{(a)} \right\rangle \\ &= [\mathbf{U}^\dagger \mathbf{f}_\alpha^{(a)} \mathbf{U} + \mathbf{U}^\dagger \frac{\partial}{\partial R_\alpha} \mathbf{U}]_{I,J} = 0. \end{aligned} \tag{2.7}$$

Thus, the solution to the partial differential equation

$$\mathbf{f}_{\alpha}^{(a)}\mathbf{U}+\frac{\partial}{\partial R_{\alpha}}\mathbf{U}=0 \tag{2.8}$$

provides a rigorous diabatic basis. It is solved starting from an arbitrary point $\mathbf{R}_0$ where the adiabatic and diabatic representations are chosen to agree, that is $\mathbf{U}(\mathbf{R}_0)=\mathbf{I}$. The nuclear Schrödinger equation in the diabatic representation is obtained from Eq. (2.4b) by changing (*a*) to (*d*), replacing the diagonal energy matrix $\mathbf{E}^{(a)}$ with $\mathbf{V}=\mathbf{U}\mathbf{E}^{(a)}\mathbf{U}^{\dagger}$ and $\mathbf{f}=\mathbf{0}$. Note that in the adiabatic basis $\mathbf{H}^e$ is diagonal, *i.e.*, adiabatic states are not coupled by $\mathbf{H}^e$ while $\mathbf{T}_N$ is diagonal in the diabatic basis, *i.e.*, the diabatic basis is not coupled by the nuclear kinetic energy. Eq. (2.8) shows that $\mathbf{f}^{(a)}$ alone defines the diabatic basis.

Hence, the existence of a rigorous diabatic basis, a basis in which $\mathbf{f}^{(d)}=\mathbf{0}$, now hinges on the existence of a solution to Eq. (2.8). This puts us in the period 1976 – 1979. Several cases arise. As pointed out by Baer, Eq. (2.8) can be solved using line integrals along a sequence of linear paths provided the curl conditions are satisfied.[36] Thus, the existence of a rigorous diabatic basis becomes equivalent to the line integral solution to Eq. (2.8) being independent of path, making **U** a proper function of nuclear coordinates.

Alternatively, we can require that the mixed partial derivatives of **U** be equal, that is

$$\frac{\partial^2}{\partial R_{\alpha}\partial R_{\beta}}\mathbf{U}=-\frac{\partial}{\partial R_{\alpha}}\left(\mathbf{f}_{\beta}^{(a)}\mathbf{U}\right)=\frac{\partial^2}{\partial R_{\beta}\partial R_{\alpha}}\mathbf{U}=-\frac{\partial}{\partial R_{\beta}}\left(\mathbf{f}_{\alpha}^{(a)}\mathbf{U}\right), \tag{2.9a}$$

which yields the curl condition, as follows. Using Eq. (2.8) in Eq. (2.9a) gives

$$(\mathbf{K}_{\alpha\beta}^{(a)}-\mathbf{K}_{\beta\alpha}^{(a)})\mathbf{U}=\left(\mathbf{f}_{\alpha}^{(a)}\mathbf{f}_{\beta}^{(a)}-\mathbf{f}_{\beta}^{(a)}\mathbf{f}_{\alpha}^{(a)}\right)\mathbf{U}, \tag{2.9b}$$

where

$$\mathbf{K}_{\alpha\beta}^{(a),I,J}(\mathbf{R}) = \left\langle \frac{\partial}{\partial R_\alpha}\psi_I^{(a)}(\mathbf{r};\mathbf{R}) \middle| \frac{\partial}{\partial R_\beta}\psi_J^{(a)}(\mathbf{r};\mathbf{R}) \right\rangle_{\mathbf{r}}. \tag{2.9c}$$

When a complete set of electronic states is inserted into eq. (2.9c), we obtain

$$\mathbf{K}_{\alpha\beta}^{(a),I,J} = \sum_{K=1}^{N^M} f_\alpha^{(a),K,I} f_\beta^{(a),K,J}. \tag{2.9d}$$

The difference between Eq. (2.9d) and the first term on the right hand side of Eq. (2.9b) is the length of the sum made explicit in Eq. (2.9d), which is N^{state} in Eq. (2.9b), and M the length of the *ab initio* expansion in Eq. (2.9d). Thus, we conclude that rigorous diabatic bases do not exist for *ab initio* wave functions for which $N^M >> N^{state}$ and the culprit is the derivative couplings to the electronic states not included in the diabatization.[42] However, for model Hamiltonians obtained using surface fitting it is possible to obtain diabatic representations which approximate the *ab initio* determined quantities but for which $N^M = N^{state}$. For the archetypical case $N^{state} = 2$ in triatomic molecules with three internal coordinates, path invariance is expressed in terms of the Hodge decomposition[53] of a vector into the sum of a gradient of a scalar $\nabla\xi$ (line integral path independent) and the curl of a vector $\nabla \times \mathbf{A}$ (line integral is path dependent).[54] Finally, the GP effect in systems exhibiting CIs makes line integrals path dependent.[36, 42, 55]

We now show how the derivative coupling is intimately related to CIs and emphasize the universality of the analysis. The immediate vicinity of all CIs can be described in terms of two directions ($3N^n$ dimensional vectors): an x-axis along $\mathbf{g}^{I,J}$ with components

$$2g_\alpha^{I,J}(\mathbf{R}) = \left\langle \psi_I^{(a)} \middle| \frac{\partial \hat{H}^e}{\partial R_\alpha} \middle| \psi_I^{(a)} \right\rangle_{\mathbf{r}} - \left\langle \psi_J^{(a)} \middle| \frac{\partial \hat{H}^e}{\partial R_\alpha} \middle| \psi_J^{(a)} \right\rangle_{\mathbf{r}}, \quad \| \mathbf{g}^{I,J} \| = g^{I,J}, \tag{2.10a}$$

and a y-axis along $\mathbf{h}^{I,J}$ with components

$$h_\alpha^{I,J}(\mathbf{R}) = \left\langle \psi_I^{(a)} \left| \frac{\partial \hat{H}^e}{\partial R_\alpha} \right| \psi_J^{(a)} \right\rangle_{\mathbf{r}}, \quad \| \mathbf{h}^{I,J} \| = h^{I,J}. \tag{2.10b}$$

and we define polar coordinates as $x = \rho\cos\theta$ and $y = \rho\sin\theta$. Here, $\mathbf{g}^{I,J}$ and $\mathbf{h}^{I,J}$ can be chosen orthogonal with no loss in generality.[56] In terms of these directions, and the trace

$$2s_\alpha^{I,J}(\mathbf{R}) = \left\langle \psi_I^{(a)} \left| \frac{\partial}{\partial R_\alpha} \mathbf{H}^e \psi_I^{(a)} \right\rangle_{\mathbf{r}} + \left\langle \psi_J^{(a)} \left| \frac{\partial}{\partial R_\alpha} \mathbf{H}^e \psi_J^{(a)} \right\rangle_{\mathbf{r}} \right., \tag{2.10c}$$

$\mathbf{H}^e$ has the form

$$\mathbf{H}^e(\mathbf{R}) = (s_x^{I,J} x + s_y^{I,J} y)\mathbf{I} + \begin{pmatrix} -g^{I,J} x & h^{I,J} y \\ h^{I,J} y & g^{I,J} x \end{pmatrix}, \tag{2.11a}$$

where

$$s_x^{I,J} = \sum_\alpha^{N^n} s_\alpha^{I,J} \frac{g_\alpha^{I,J}}{\left\| \mathbf{g}^{I,J} \right\|} \quad \text{and} \quad s_y^{I,J} = \sum_\alpha^{N^n} s_\alpha^{I,J} \frac{h_\alpha^{I,J}}{\left\| \mathbf{h}^{I,J} \right\|}. \tag{2.11b}$$

Diagonalizing $\mathbf{H}^e$ gives the energies and derivative couplings, which are

$$\varepsilon = \frac{1}{2}(s_x^{I,J} x + s_y^{I,J} y) \pm \rho\Lambda, \tag{2.12a}$$

$$f_\theta^{(a),I,J}(\mathbf{R}) = \frac{g^{I,J} h^{I,J}}{2\Lambda^2}, f_\rho^{(a),I,J}(\mathbf{R}) = 0 \tag{2.12b}$$

$$\Lambda = \left[\left(g^{I,J} \cos\theta \right)^2 + \left(h^{I,J} \sin\theta \right)^2 \right]^{1/2}. \tag{2.12c}$$

It is important to note that from Eq. (2.12b) in polar coordinates neither of the derivative couplings is singular at the point of a CI as is always (correctly) stated. The singularity arises from the $1/\rho$

that accompanies the θ derivative. Note too that from Eq. (2.12a) $\rho \sim$ the electronic energy difference, as expected.

2.3. Spin-Orbit Coupling

CIs promote spin conserving nonadiabatic dynamics, namely IC. When the nonadiabatic event involves a change in the total electronic spin state, namely ISC, the SOC must be involved. In this perspective, we will treat the SOC using the Breit-Pauli approximation,[14] which is given below

$$\hat{H}^{SO} = \sum_{i=1}^{N^e} \mathbf{h}_i^{SO} \cdot \mathbf{s}_i - \sum_{i,j=1}^{N^e} \mathbf{h}_{ij}^{SOO} \cdot (\mathbf{s}_i + 2\mathbf{s}_j), \tag{2.13a}$$

with

$$\mathbf{h}_i^{SO} = \frac{1}{2c^2} \sum_{\alpha=1}^{N^n} \frac{Z_\alpha}{r_{i,\alpha}^3} \left(\mathbf{r}_{i,\alpha} \times \mathbf{p}_i \right), \tag{2.13b}$$

$$\mathbf{h}_{ij}^{SOO} = \frac{1}{2c^2} \frac{\mathbf{r}_{i,j} \times \mathbf{p}_i}{r_{i,j}^3}. \tag{2.13c}$$

In this case, the electronic Hamiltonian is given by $\hat{H}^E = \hat{H}^e + H^{SO}$. We incorporate this interaction in the spin-diabatic approximation. See below. We further restrict ourselves here to molecules with even numbers of electrons. In this case the Hamiltonian matrix will be real-valued owing to time reversal symmetry. When the number of electrons is odd, the off-diagonal matrix elements may be complex, complicating the analysis.[57] Below we provide, as an example, construction of the relativistic electronic Hamiltonian for the frequently used 2 singlets and 1 triplet 5 dimensional space, which is readily extended to (n singlets and m triplets).

The spin-orbit coupling matrix elements are initially built in the adiabatic basis and then transformed using

$$\boldsymbol{\psi}^{(d),S,M_S} = \mathbf{U}^S \boldsymbol{\psi}^{(a),S,M_S} . \tag{2.14}$$

to the diabatic representation so they can be fit by neural networks. Note the transformation is independent of M_S, The electronic basis states are thus the diabatized electronic singlet states and theadiabatic triplet state The state label J in $\psi_J^{(e)}$ is replaced by S, M_S giving $\psi_J^{(e),S,M_S}$ where $S(S+1)$ is the eigenvalue of S^2 and M_S = -S, -S+1, …, S is the azimuthal spin quantum number, with multiplicity 2S+1. Only the singlet spin block of the Hamiltonian is diabatized.

Here with the I^{th} nonrelativistic energy with spin symmetry S, M_s denoted $E_I^{(a),I,S,p,(m)}$ and $\left\langle \psi_I^{(a),S,M_S} \left| \hat{H}^{SO} \right| \psi_J^{(a),S',M_{S'}} \right\rangle_{\mathbf{r}} = \left\langle IS^{M_S} \left| JS'^{M_{S'}} \right\rangle \right.$, $\mathbf{H}^E$ (the electronic Hamiltonian) has the following form in the adiabatic basis

$$\begin{pmatrix} E^{(a),1,0,0,(m)} & & & & \\ 0 & E^{(a),2,0,0,(m)} & & & \\ <10^0|1^+> & <20^0|1^+> & E^{(a),1,1,1^+,(m)} & & \\ <10^0|1^0> & <20^0|1^0> & 0 & E^{(a),2,1,0,(m)} & \\ <10^0|1^-> & <20^0|1^-> & 0 & 0 & E_1^{(a),3,1,1^-,(m)} \end{pmatrix}. \tag{2.15}$$

This matrix is then transformed to the diabatic basis, the basis in which the DPEM and the $\left\langle IS^{M_S} \left| JS'^{M_{S'}} \right\rangle \right.$ are fit. For more details on the construction and use of eq. (2.15) see Section 4.4.

3. Diabatization

3.1 Different Diabatization Schemes

Diabatization is the process of constructing diabatic bases. For polyatomic molecules, which are the main interest here, rigorous diabatization does not exist,[36, 37] as discussed above. The fact that diabatic bases are not uniquely defined has given rise to a wide variety of diabatization methods, all approximate for polyatomic systems. These methods can be categorized according to the type of information on which the diabatization is based. Each type of methods has its own advantages and drawbacks of one form or another.

The first type of diabatization methods is derivative-based, which is in principle the most quantifiable approach as they directly use the derivative couplings to diabatize electronic states, in addition to energy (and sometime gradients). Existing derivative-based methods include (i) solution of the Poisson equation,[58, 59] (ii) the Shepard interpolation,[60-62] (iii) line integral methods.[63-65] One challenge of derivative-based methods is that derivative couplings are rarely computed analytically, especially those from high-level post-Hartree-Fock wavefunctions, while numerical calculations are quite expensive.

Alternatively, diabatization can be performed using molecular properties of the molecular system of interest. The basic premise is that molecular properties in diabatic bases should be a smooth and continuous function of the nuclear coordinates. Almost any real-valued Hermitian operator, such as dipole moment and quadrupole moment, satisfying only certain restrictions, can be used to produce a diabatic representation that removes the singularity of the derivative coupling near a CI.[66] One classic example is the generalized Mulliken-Hush method, which is based on the charge of the molecule.[67, 68] Other properties used in diabatization include dipole, quadrupole, and other electrostatic properties,[69-71] as well as other molecular properties.[72] One major advantage of property-based methods is that the relevant molecular properties can be obtained readily from electronic wavefunctions with very limited computation effort. Even for electronic structure

methods that do not explicitly provide wavefunctions, this strategy can still be useful.[73] In addition, they are direct or point-wise methods, which means that the diabatization at different geometries can be done separately. Due to their simplicity, property-based methods have been widely used. However, the quality of property-based diabatization cannot be strictly controlled and depends to a large extent on the relevant molecular property. The most deleterious drawback of property-based methods is the possibility of diabolical singularities,[74-76] which are the artificially fallacious singularities in the derivative coupling, although methods for mitigating their effects have been proposed.[76, 77]

Another widely used type of diabatization approach is the diabatization by *ansatz*, which is reproduced by fitting with a physically inspired DPEM model. An exemplary application of diabatization by *ansatz* is the vibronic coupling approach,[7] in which the DPEM is expressed with only a low (first or second) order Taylor expansion of the normal coordinates around a reference geometry. Adiabatic energies can then be used to determine the expansion coefficients - derivative couplings are not needed. The major drawback of vibronic coupling approach is that it is only valid in a small region around the reference point, due to the pre-specified functional form of the model Hamiltonian and thus unable to describe chemical processes involving bond breaking and forming. To describe more extended regions, higher-order expansions of this approach have been proposed by several groups.[78-82] More recently, artificial neural networks (NNs) have been incorporated into the *ansatz* to make vibronic coupling models more general and flexible.[83-85] In addition to vibronic coupling approach, other forms of DPEM model for smaller systems were also reported.[86-88] Furthermore, methods based on the Diatomics-in-Molecules (DIM) model,[89] which add many-body terms to the elements of the DIM matrix, were used to deal with charge transfer reactions.[90-92] However, even with more flexible functional forms, the success is not guaranteed as the

diabatization still depends on the assumptions embedded in the *ansatz*. In situations where an *ansatz* cannot be found, for example, diabatization is impossible.

Diabatization can also be achieved by directly exploiting the electronic wavefunctions, among which the most widely used is the block diagonalization.[93-95] The basic principle here is the configurational uniformity,[96, 97] which is based on the premise that the dominant character of a diabatic state can be expressed as a single configuration state function (CSF) or a linear combination of CSFs, which is preserved as the configurational space evolves. A variety of hybrid methods have also been proposed, such as the hybrid method of block-diagonalization and diabatization by *ansatz*.[98] A similar approach takes advantage of the similarities of wavefunctions to perform the diabatization.[99-101] The regularized diabatization introduced by Thiel and Koppel removes the singularity at the conical intersection and gives the adiabatic result at large separations.[99-102]

Zhu and Yarkony recently proposed a simultaneous Fitting-and-Diabatizing (FaD) method,[103, 104] which can also be viewed as a hybrid method of derivative-based diabatization and diabatization by *ansatz*. In the FaD method, the DPEM is expressed with symmetrized functional form, *i.e.*, the *ansatz*, spanned by symmetry-adapted polynomials (SAPs)[103, 104] or NNs,[105] which will be discussed in more detail in the next section. *Ab initio* electronic structure data including energies, energy gradients, and derivative couplings are simultaneously fit and diabatized to generate a robust and accurate quasi-diabatic representation. Since derivative couplings are used to diabatize electronic states, the residual derivative couplings can be determined and used to assess the quality of the diabatization so that the quality of diabatization is strictly under control. Including the energy gradients can help to reduce the number of geometries needed to saturate the configuration space. With **g** and **h** vectors being fit, the local topology of a CI is also reproduced

automatically.[106] Therefore, this method ultimately provides an accurate, quantifiably quasi-diabatic representation in a least-square sense. More details concerning FaD method are provided in Sec. 4.3. In Sec. 6, some examples will be discussed in the context of direct comparison with experimentally measured dynamical attributes in photodissociation and reactive scattering.

4. Diabatic Potential Energy Matrices

4.1. Complete Nuclear Permutation and Inversion Symmetry

Since symmetry operators commute with the Hamiltonian, it is advantageous to take into consideration the symmetry properties of the system. In many cases, symmetry adaption is a necessity if the spectrum and dynamics are to be described correctly. Chemical reactions involve the breaking and forming of chemical bonds, in which molecules undergo large amplitude motion, so that point group symmetry is often inadequate. The appropriate symmetry group describing a molecular system in the entire configuration space is the complete nuclear permutation and inversion (CNPI) group.[107] To construct a global DPEM that can describe chemical reactions, the CNPI symmetry must be embedded in the functional form of DPEM. When the CNPI group is too large to handle, it is often sufficient to use only a subgroup to preserve part of the symmetry.[108]

Once the CNPI group is determined for a molecular system, its irreducible representations can be constructed unambiguously using group theory. For a certain irreducible representation, the wavefunction (or matrix element) transforms accordingly under the operations of the symmetry group. As for an individual block of a DPEM

$$\mathbf{H}^{d}_{\alpha,\beta}(\mathbf{R}) \equiv \left\langle \psi^{(d)}_{\alpha}(\mathbf{r};\mathbf{R}) \middle| \hat{H}^{e}(\mathbf{r};\mathbf{R}) \middle| \psi^{(d)}_{\beta}(\mathbf{r};\mathbf{R}) \right\rangle_{\mathbf{r}}, \tag{4.1}$$

it will transform as $\Gamma(\psi_\alpha^{(d)})\otimes\Gamma(\psi_\beta^{(d)})$, where Γ denotes an irreducible representation. The analytical representation of PEM must adhere to its transformation properties to correctly account for the global CNPI symmetry. For simplicity, only one-dimensional (1D) irreducible representations are discussed here.

4.2. Representation of the DPEM

DPEM elements should be smooth and continuous functions of molecular internal coordinates. This is the very same premise as in the construction of adiabatic PESs except near CIs.[109-111] Therefore, a variety of machine learning techniques used for the analytical representation of adiabatic PESs can be borrowed to construct DPEM, as long as correct CNPI symmetry adaptation can be applied. Such techniques include simple interpolation,[112, 113] modified Shephard interpolation by Collins and co-workers,[60-62] double many-body expansion of Varandas,[114] SAPs by Zhu and Yarkony,[103, 104, 115] and more recent NN based methods with a symmetrized input layer.[105, 116]

To correctly symmetrize the analytical representation, Zhu and Yarkony proposed a general projection operator method generating SAP expansions to represent the DPEM elements. The projection operator for the μth (1D) irreducible representation of the CNPI group takes following form

$$\hat{P}^{\mu} = \frac{1}{O_G}\sum_x \Gamma^{(\mu)}(x)^* \hat{x}, \qquad (4.2)$$

where O_G is the number of group elements, $\hat{x}$ is the group operator for the corresponding group element x, and $\Gamma^{(\mu)}(x)$ is the irreducible character of x. Apply $\hat{P}^{\mu}$ to the monomials of basic internal coordinates, the terms that survive will transform as the μth irreducible representation. The reader can find a simple example of how projection operators are used in Ref. [104].

More recent efforts to analytically express DPEMs include the use of permutation-invariant polynomials (PIPs) and artificial NNs. The PIPs can be viewed as a special case of a projection operator method. The basic coordinates employed in PIPs are the internuclear distances, and the corresponding projection projector is that of the totally symmetric irreducible representation. The use of internuclear coordinates, rather than internal coordinates, have important advantages, as the permutations can be readily enforced.[109] On the other hand, artificial NNs are a universal and robust fitting tool, which are extremely flexible and can thus represent discrete data to very high accuracy.[117] The combination of PIPs and NNs, *i.e.*, the PIP-NN method,[118, 119] and the related fundamental invariant NN (FI-NN) method,[120] in which the NN takes PIPs as the input, has been successfully applied to the construction of reactive adiabatic PESs for polyatomic molecules in the gas phase and for the interaction of small molecules with metal surfaces.[5, 6, 121] It provides a simple and rigorous procedure to correctly account for the totally symmetric property of adiabatic PESs.

PIP-NN can be readily used to express totally symmetric blocks of a DPEM. As for the other symmetric blocks, one can still take advantage of the PIP-NN. In general, a DPEM block that transforms as the μth irreducible representation, can be expressed by[116]

$$\sum_i Q_i^{(\mu)} \cdot \mathrm{NN}_i(\mathrm{PIP}), \tag{4.3}$$

where $Q_i^{(\mu)}$ are the symmetry adapted coordinates obtained by the projection projector method and $\mathrm{NN}_i(\mathrm{PIP})$ are NN functions with PIPs as input. When the μth irreducible representation is totally symmetric, $Q_i^{(\mu)}$ can be reduced to 1. For non-totally-symmetric irreducible representations, the $Q_i^{(\mu)}$ term (and its higher order terms that preserve the same symmetry) enforces the corresponding permutation symmetry. The functional form not only preserves the correct symmetry, but also provides the functional flexibility to fit via NN functions. It has been successfully applied to the

DPEMs of ammonia[105, 116] and formaldehyde[122, 123] and exhibited its powerful fitting capacity, as evinced by the small fitting errors and accurate dynamical results. However, artificial NNs do have disadvantages. NNs tend to overfit easily due to their highly flexible functional forms. The lack of physical meaning in the NN functional form leads to very limited extrapolation capability. Therefore, to accurately describe a chemical system with an NN method, it is indispensable to saturate the relevant regions with *ab initio* calculations, which can be very time-consuming for larger systems. For a more comprehensive review of the advantages and disadvantages of artificial NNs, the readers are referred to Ref. [124].

4.3 Fitting-and-Diabatizing Method

Accompanying DPEM $\mathbf{H}^d$ is following electronic Schrödinger equation,

$$\left[\mathbf{H}^d(\mathbf{R}) - \mathbf{I}E^{a,J,(m)}\right]\mathbf{d}^J(\mathbf{R}) = \mathbf{0}, \tag{4.4}$$

where $\mathbf{I}$ is the identity matrix and $E^{a,J,(m)}$ is the corresponding eigenenergy. The superscript (m) indicates that the results come from the model Hamiltonian $\mathbf{H}^d$, rather than ab initio (ab) calculations, and the superscript (a) indicates the adiabatic representation. The AtD transformation is given by eigenvectors $\mathbf{d}^J(\mathbf{R})$.

The analytical symmetrized DPEM representing N^{state} adiabatic electronic states presented in Sec. 4.2 contains a set of adjustable nonlinear parameters $\boldsymbol{\lambda}$, which are determined by a least squares fitting procedure to reproduce *ab initio* determined energies, energy gradients, and interstate couplings. For *ab initio* data (ab), define

$$L_0^{I,I,(ab)}(\mathbf{R}) = E^{a,I,(ab)}(\mathbf{R}), \tag{4.5a}$$

$$L_k^{I,I,(ab)}(\mathbf{R}) = \nabla_k E^{a,I,(ab)}(\mathbf{R}), \tag{4.5b}$$

$$L_k^{I,J,(ab)}(\mathbf{R}) = h_k^{a,I,J,(ab)}(\mathbf{R}), \tag{4.5c}$$

where k labels gradient (coupling) component. $h_k^{a,I,J,(ab)}$ is interstate coupling defined as $h_k^{a,I,J,(ab)} = (E^{a,J,(ab)} - E^{a,I,(ab)}) f_k^{a,I,J,(ab)}$, which exhibits no singularity and thus can be fit. The expressions for the $\mathbf{H}^d$ determined (m) counterparts are

$$L_0^{I,I,(m)}(\mathbf{R}) = \mathbf{d}^I(\mathbf{R})^\dagger \mathbf{H}^d \mathbf{d}^I(\mathbf{R}), \tag{4.6a}$$

$$L_k^{I,I,(m)}(\mathbf{R}) = \mathbf{d}^I(\mathbf{R})^\dagger \nabla_k(\mathbf{H}^d) \mathbf{d}^I(\mathbf{R}), \tag{4.6a}$$

$$L_k^{I,J,(m)}(\mathbf{R}) = \mathbf{d}^I(\mathbf{R})^\dagger \nabla_k(\mathbf{H}^d) \mathbf{d}^J(\mathbf{R}), \tag{4.6a}$$

To obtain the optimal parameters, the following loss function is minimized,

$$P(\boldsymbol{\lambda}) = \frac{1}{2}\sum_{n=1}^{N^{lsq}} \left[w_n (L_n^{(m)} - L_n^{(ab)})\right]^2 + \frac{1}{2} t \boldsymbol{\lambda}^\dagger \boldsymbol{\lambda}, \tag{4.7}$$

where N^{lsq} is the number of least squares terms and w_n is the weight for each least squares term. The regularization term $\frac{1}{2} t \boldsymbol{\lambda}^\dagger \boldsymbol{\lambda}$ is added to avoid over-fitting, where t is a small positive factor (e.g., 10^{-7}).

4.4. Representation of Scalar and Vector Properties

Molecular properties, such as the SOC and dipole moments, may not be smooth functions of nuclear coordinates in the adiabatic representation near an electronic degeneracy, such as a CI seam, because of the sudden switch of the electronic character. To provide a globally accurate representation of such properties, a diabatic representation is desired. For a molecular system, after a proper diabatization has been constructed, molecular properties for the same adiabatic states can also be diabatized with the same AtD transformation. Let us consider an Hermitian molecular property operator $\hat{O}$, its matrix forms in adiabatic and diabatic bases are

$$\mathbf{O}_{\alpha,\beta}^{(a)}(\mathbf{R}) \equiv \left\langle \psi_{\alpha}^{(a)}(\mathbf{r};\mathbf{R}) \middle| \hat{O}(\mathbf{r};\mathbf{R}) \middle| \psi_{\beta}^{(a)}(\mathbf{r};\mathbf{R}) \right\rangle_{\mathbf{r}}, \tag{4.8a}$$

$$\mathbf{O}_{\alpha,\beta}^{(d)}(\mathbf{R}) \equiv \left\langle \psi_{\alpha}^{(d)}(\mathbf{r};\mathbf{R}) \middle| \hat{O}(\mathbf{r};\mathbf{R}) \middle| \psi_{\beta}^{(d)}(\mathbf{r};\mathbf{R}) \right\rangle_{\mathbf{r}}, \tag{4.8b}$$

where **r** and **R** are the electronic and nuclear coordinates, respectively. $\mathbf{O}^{\mathrm{d}}$ and $\mathbf{O}^{\mathrm{a}}$ are linked by the same AtD transformation

$$\mathbf{O}^{(d)} = \mathbf{U}\mathbf{O}^{(a)}\mathbf{U}^{\dagger}. \tag{4.9}$$

As discussed above, the discontinuities of $\mathbf{O}^{(a)}$ due to a CI seam can be removed by AtD transformation, rendering $\mathbf{O}^{(d)}$ smooth and continuous in the configuration space. Thus, an analytical representation will also be feasible for $\mathbf{O}^{(d)}$ and thus $\mathbf{O}^{(a)}$.

The SOC between electronic states with different spin multiplicities is a scalar property that is responsible for the nonadiabatic ISC process. The SOCs in the adiabatic representation have discontinuities near a CI seam, due to sudden change of electronic character, thus impossible to represent by an analytic function. Diabatization helps to remove such discontinuities and render the transformed SOCs amenable for an analytical representation, thus providing a unified description of both IC and ISC in the same diabatic framework.

Let us consider a system in which IC and ISC compete. The system is comprised of N^S electronic states of total electron spin S, ($\psi_i^{(a),S,M_S}(\mathbf{r};\mathbf{R})$, $i = 1,\cdots,N^S$, $M_S = -S, -S+1,\cdots,S-1,S$) and $N^{S'}$ electronic states of spin multiplicity S' ($\psi_j^{(a),S',M_{S'}}(\mathbf{r};\mathbf{R})$, $j = 1,\cdots,N^{S'}$, $M_{S'} = -S', -S'+1,\cdots,S'-1,S'$). Distinct diabatizations can be performed within the two spin manifolds,[125]

$$\boldsymbol{\psi}^{(d),S,M_S} = \mathbf{U}^{S}(\mathbf{R})\boldsymbol{\psi}^{(a),S,M_S}, \tag{4.10a}$$

$$\boldsymbol{\psi}^{(d),S',M_{S'}} = \mathbf{U}^{S'}(\mathbf{R})\boldsymbol{\psi}^{(a),S',M_{S'}}. \tag{4.10b}$$

The diabatized SOC matrix will take following form

$$\left\langle \boldsymbol{U}^{S}(\mathbf{R})\boldsymbol{\psi}^{(a),S,M_S} \middle| \hat{H}_{SO} \middle| \boldsymbol{U}^{S'}(\mathbf{R})\boldsymbol{\psi}^{(a),S',M_{S'}} \right\rangle, \tag{4.11}$$

where $\hat{H}_{SO}$ is the SOC operator in the Breit-Pauli approximation. The elements of diabatized SOC matrix are thus linear combinations of adiabatic SOCs. This strategy has recently been successfully demonstrated for ammonia[126] and formaldehyde.[123]

The CNPI symmetry of $\mathbf{O}^{(d)}$ can be determined in a manner similar to that used for $\mathbf{H}^{e}$. According to Eq. (4.2), $\mathbf{O}^{d}_{\alpha,\beta}$ will transform as $\Gamma(\psi_{\alpha}^{(d)})\otimes\Gamma(\hat{O})\otimes\Gamma(\psi_{\beta}^{(d)})$. For scalar molecular properties, the symmetrized analytical representation for DPEM blocks can be readily used without too many modifications. However, when it comes to vector properties, such as electric dipole moments, special care must be taken to deal with the translational and rotational DOFs.

Normally, vector properties are invariant with respect to translation or have very simple transformation properties. Consequently, the translational DOF can be simply removed by fixing one special point in space, such as the center of mass and or a special atom. As for the rotational DOFs, the vector properties are often covariant with the rotation, thus require a special treatment. Typically, a special axis system can be introduced to place the molecule at a specific orientation. With the translational and rotational DOFs being removed, the diabatized vector molecular properties will be smooth and continuous functions of nuclear coordinates, thus enabling an analytical representation. This has been demonstrated recently by a diabatic representation of the electric dipole moments of 1,2 ^{1}A states of ammonia.[127]

4.5. Phase Problems in Diabatization

Most quantum chemistry programs employ real wavefunctions, and it is well known that the wavefunctions have random signs (phases). This does not affect energies or energy gradients. However, any off-diagonal elements, such as derivative couplings, transition dipole moments, and SOCs, will change sign if one of the two state wavefunctions changes sign. In derivative-based diabatizations, the random sign change of derivative couplings leads to fictious discontinuities, which must be removed in order to obtain a smooth diabatic representation. For chemical systems with small numbers of internal DOFs, such as triatomic systems, the arbitrariness in derivative coupling can be removed by checking its smoothness on grids. However, this is not possible for larger systems. Instead, Collins and coworkers, in their modified Shepard interpolation method, had made the signs of the derivative couplings consistent by comparing the interpolation of the diabatic PEM between adjacent data points.[60] In the FaD method, a different approach was adopted. During each iteration of the fitting, the signs of $\boldsymbol{d}^J$ are adjusted, and the sign combination that makes model determined interstate couplings $h_k^{a,IJ,(m)}$ closest to the *ab initio* counterparts $h_k^{a,IJ,(ab)}$ is chosen.[103] By this way, the signs of $h_k^{a,IJ,(m)}$ are made consistent with those of $h_k^{a,IJ,(ab)}$.

For property-based methods and the diabatization of molecule properties and interactions, the arbitrariness in the sign of the off-diagonal element will also lead to fictious discontinuities. In order to achieve sign consistency, a cluster growing algorithm has been introduced.[128] The algorithm begins with an initial cluster, for which the sign consistency has been achieved by for example examining the functional smoothness on grids or choosing a region without off-diagonal element passing through zero. Then, the diabatic Hamiltonian or the diabatized properties and interactions in the cluster are fitted with analytical models. The signs of nearby points can then be determined by comparing the predictions of the analytical model and the values from *ab initio* data

with different sign combinations. The newly determined points are then added into the cluster. After each iteration, the cluster grows, hence the name "cluster growing".

The validity of the cluster growing algorithm hinges on the smoothness of the diabatic Hamiltonian or the diabatized properties and interactions and the capability of the analytical model to extrapolate. The smoothness can be guaranteed as long as the diabatization methods are valid. As for the extrapolation, physically motivated functional form is the best option, however, for complex systems, coming up with a suitable and accurate functional form is tedious and not an easy task. A universal solution is the Gaussian Process Regression,[129] which has been used to diabatize dipole moments and SOCs.[127] In addition, the nearby points have to be carefully chosen, which is usually based on a distance criterion or a cutoff threshold. The cutoff threshold should not be too large, because the extrapolation of analytical model may not be reliable at points far away from the current cluster.

5. Quantum Nonadiabatic Dynamics

5.1. The Hamiltonian and Discretization

For a molecule with N^n atoms, there are $3N^n$-6 internal DOFs. In full-dimensional quantum Hamiltonians, the selected coordinates need to cover all internal DOFs in the system. We will discuss below general coordinates used in simulating the photodissociation of the molecules for triatomic and tetratomic systems in full dimensionality and several typical polyatomic systems with N^n>4 in reduced dimensional models. For collisional processes, detailed descriptions of the coordinates and discretization can be found in a number of reviews,[130-133] so not repeated here. In most cases, a multi-state nuclear Hamiltonian of a system can be written in a diabatic representation as:

$$\mathbf{H}^T = \mathbf{T}_N + \mathbf{V} = \sum_{I=1}^{N^{state}} |I\rangle \hat{T}_N \langle I| + \sum_{I,J=1}^{N^{state}} |I\rangle V_{IJ} \langle J|, \quad (5.1)$$

in which $\mathbf{T}_N$ is the nuclear kinetic energy operator (KEO) and diagonal, and $\mathbf{V}$ is the potential energy operator (PEO) in a diabatic representation as the DPEM, which includes the couplings between the diabatic electronic states in its off-diagonal terms. $\mathbf{V}$ is the function of the nuclear coordinates of the system and can be easily and directly represented in a grid. However, the form of $\mathbf{T}_N$ is dependent on the coordinate chosen.

In photodissociation, the dynamics is often weakly dependent on the overall rotation. As a result, it is often sufficient to consider zero total angular momentum (J=0).[17] Extension to non-vanishing J is straightforward. For a triatomic system ABC, the Jacobi coordinates (R, r, θ) are commonly used because they give a natural description of the product channel (say A + BC), and the three-dimensional (3D) KEO is given by ($\hbar = 1$):[134]

$$\hat{T}_N = -\frac{1}{2\mu_R}\frac{\partial^2}{\partial R^2} - \frac{1}{2\mu_r}\frac{\partial^2}{\partial r^2} + \frac{\hat{j}^2}{2\mu_R R^2} + \frac{\hat{j}^2}{2\mu_r r^2}, \quad (5.2)$$

in which R is the distance between A and the center of mass of BC, r is the bond length of the diatom BC, and θ is the angle between the vectors $\mathbf{R}$ and $\mathbf{r}$. μ_R and μ_r are the corresponding reduced masses, respectively. j is the rotational angular momentum of the diatom.

When the number of the atoms in the molecule goes up to four, the full quantum dynamics at the state-to-state level become significantly more challenging due to the inclusion of six internal DOFs and a large number of energetically available product states in general. There are a variety of coordinates systems for tetratomic molecules,[135] but the choice depends on the nature of the product channels. For an A + BCD type product channel, for example, the atom-triatom Jacobi

coordinate system is ideal for computing the product ro-vibrational state distributions.[136] In this coordinate system, the KEO (J=0) of the tetratomic molecule ABCD can be written as:[135]

$$\hat{T}_N = -\sum_{i=1}^{3} \frac{1}{2\mu_i} \frac{\partial^2}{\partial r_i^2} + \frac{\hat{j}_1^2}{2\mu_1 r_1^2} + \frac{(\hat{j}_1^2 + \hat{j}_2^2)^2}{2\mu_2 r_2^2} + \frac{\hat{j}_2^2}{2\mu_3 r_3^2}, \tag{5.3}$$

in which r_1 is the bond length of diatom AB, r_2 is the distance from the center of mass of diatom AB to atom C as discussed above in triatomic system, and r_3 is the distance from the center of mass of triatom ABC to atom D. μ_1, μ_2, and μ_3 are the corresponding reduced masses. $\hat{j}_1$ and $\hat{j}_2$ are the angular momentum operators for diatom AB and triatom ABC, respectively.

If the triatomic product has symmetry, such as in the photodissociation of ammonia (NH_3 + $h\nu \rightarrow$ NH_2 + H), the (2+1) Radau-Jacobi coordinates are optimal to express the Hamiltonian for computing the absorption spectrum[137, 138] and the product branching ratios.[139] The KEO in this coordinate system can be written as:[140]

$$\hat{T}_N = -\sum_{i=0}^{2} \left(\frac{1}{2\mu_i} \frac{\partial^2}{\partial r_i^2} + \frac{\hat{j}_i^2}{2\mu_i r_i^2} \right), \tag{5.4}$$

where r_0 is radial Jacobi coordinate between the atom and triatomic center of mass, r_1 and r_2 are two radial Radau coordinates.[141] μ_i is the corresponding atomic mass associated with r_i. j_1 and j_2 are the angular momentum operators for r_1 and r_2, respectively, and $\hat{j}_0^2 = (\hat{j}_1 + \hat{j}_2)^2$.

If the products are diatoms (AB + CD), the diatom-diatom Jacobi coordinate system[135] is a better choice for describing the diatomic ro-vibrational DOFs. For J=0, the KEO has the same form as that in the (2+1) Radau-Jacobi coordinates (Eq. (5.4)), but the definitions of the radial coordinates are different. In the diatom-diatom Jacobi coordinate system, r_1 and r_2 are the diatomic

bond lengths, r_0 is the distance between the center of masses of the two diatoms. The reduced masses are also defined accordingly.

For larger molecular systems (N>4), the KEO expressed by Jacobi coordinates becomes much more complicated because of more DOFs involved in the system.[142, 143] Exact full-dimensional quantum dynamics calculations are extremely demanding. One solution to the problem is to take advantage of the multi-configurational time-dependent Hartree (MCTDH) approximation.[144] Since a time-dependent basis in the form of a Hartree product is used, the scaling of the problem is significantly less steep than the conventional grid based methods. However, an efficient implementation of MCTDH requires the PEO in the sum of product form to facilitate the calculation of the potential energy matrix along the propagation.[144] The refitting of the PESs in such a form is a major undertaking, especially for high-dimensional systems. However, recent progress in this direction has been very encouraging.[145, 146] We note in passing that the MCTDH can be further approximated using Gaussian basis, enabling a classical trajectory-like description of the dynamics. However, the so-called variational multiconfiguration Gaussian (vMCG) approach[147] is only accurate for short time dynamics, and thus not discussed here. For more details of the method, the reader is referred to an excellent review by Richings et al.[148] In addition, the ring-polymer molecular dynamics (RPMD) method can be employed to simulate the nonadiabatic reactions quantum mechanically,[149, 150] but limited to the dynamics at the product-states unresolved level. If quantum effects were unimportant, the classical methods would be appropriate as well, as discussed in the perspective by Tully.[13] Here we focused on the treatments at the quantum product-states resolved level, thus not discuss more expandingly.

An alternative approach to solving the problem is to utilize reduced-dimensionality (RD) models. This is particularly suitable for photodissociation where the dynamics is often restricted

to a few modes. In RD quantum models, the choice of the coordinate system depends largely on the problems to be resolved in practice. Typically, a few active modes are explicitly treated with an approximate KEO, while the spectator modes are either treated as normal modes, or ignored entirely. Here, we illustrate this approach using two examples, namely the photodissociation of phenol (C_6H_5OH) and the hydroxymethyl radical (CH_2OH).

In the photodissociation of phenol: $C_6H_5OH + h\nu \rightarrow C_6H_5O + H$, for example, the distance between H and the phenoxyl fragment (R) must be included. In addition, two disappearing modes,[151] namely the CCOH dihedral angle (φ) and the COH bend (θ) coordinates are also necessary in order to describe the rotation of the phenoxyl product.[152] The KEO of this RD model can be written as:

$$\begin{aligned}\hat{T}_N &= -\frac{1}{2\mu}\left(\frac{\partial^2}{\partial R^2}+\frac{1}{R^2\sin\varphi}\frac{\partial}{\partial\varphi}\sin\varphi\frac{\partial}{\partial\varphi}+\frac{1}{R^2\sin^2\varphi}\frac{\partial^2}{\partial\theta^2}\right)-\sum_i\frac{\omega_{Q_i}}{2}\frac{\partial^2}{\partial Q_i^2}\\ &= -\frac{1}{2\mu}\frac{\partial^2}{\partial R^2}+\frac{\hat{j}^2}{2\mu R^2}-\sum_i\frac{\omega_{Q_i}}{2}\frac{\partial^2}{\partial Q_i^2},\end{aligned} \tag{5.5}$$

where $\mu = m_{\mathrm{H}} m_{\mathrm{C_6H_5O}} / (m_{\mathrm{H}} + m_{\mathrm{C_6H_5O}})$, j is the rotational angular momentum of the phenoxyl moiety. This model implicitly assumes that the remaining vibrational modes in phenol can be approximated by uncoupled normal modes (Q_i), for which the frequencies are given by ω_{Q_i} while the corresponding potentials are from the DPEM and only approximately quadratic. In the original three-dimensional (3D) study, the last term in Eq. (5.5) was ignored,[152] which assumes these normal modes are identical to those in the phenoxyl product. In a subsequent study, one additional normal model was explicitly included, shedding light on its involvement in the dissociation dynamics.[153]

In another example, the photodissociation of hydroxymethyl radical: $CH_2OH + h\nu \rightarrow H_2CO + H$, was described by a four-dimensional (4D) quantum model,[154] in which the all three disappearing coordinates (R, θ, ϕ) as in the case of phenol and the C-O stretch coordinate (r) are included. The latter was important as it is strongly coupled with the dissociation coordinate. The expression of the rotationless (J=0) KEO described can be written as:

$$\hat{T}_N = -\frac{1}{2\mu_R}\frac{\partial^2}{\partial R^2} - \frac{1}{2\mu_r}\frac{\partial^2}{\partial r^2} + \frac{\hat{j}^2}{2\mu_R R^2} + \hat{K}^{rot}, \tag{5.6a}$$

where r is the distance between the CH_2 center of mass and O atom, R is the distance between the H_2CO center of mass and the dissociative H atom, θ is the angle between R and the inertial axis I_a of H_2CO, and ϕ is the out of plane angle of the dissociative H atom. $\mu_r = m_O m_{CH_2}/(m_O + m_{CH_2})$ and $\mu_R = m_H m_{CH_2O}/(m_H + m_{CH_2O})$ are the corresponding reduced masses. j is the rotational angular momentum of H_2CO. The rotational KEO of H_2CO can be approximated as:

$$\hat{K}^{rot} = \frac{\hat{j}_a^{\,2}}{2I_a} + \frac{\hat{j}_b^{\,2}}{2I_b} + \frac{\hat{j}_c^{\,2}}{2I_c}, \tag{5.6b}$$

where I_a, I_b, and I_c are the moments of inertia and they are the functions of r. As in the case of phenol photodissociation, additional normal modes can be included in the KEO to examine the dynamics in a higher dimensional phase space.[155]

While the aforementioned Hamiltonians are suitable for nonadiabatic systems coupled by derivative or spin-orbit coupling, there are some cases where the coupling between electronic and nuclear angular momenta is responsible for nonadiabatic dynamics. The Renner-Teller coupling is such a case in which the electronic orbital angular momentum couples with the molecular rotational angular momentum. Additional couplings between the electronic spin and orbital

angular momentum further complicate the situation. Such angular momentum couplings needs be treated properly, which result in terms in the KEO that require special angular basis consisting of both the electronic and nuclear quantum numbers,[156-158] complicating the treatment of the nonadiabatic dynamics.

In numerical implementation of the quantum dynamical calculations, the Hamiltonian is often discretized in direct product discrete variable representation (DVR) and/or finite basis representation (FBR).[159] Such an approach is advantageous because the KEO becomes sparse in FBR and the PEO is diagonal in DVR, so that no quadrature is needed for the PEM. The transformation between the two representations is carried out sequentially using one-dimensional transformation matrices (partial summation), which typically scales as $N\log N$ where N is the number of the total DVR points or FBR basis functions.[159] For non-dissociative coordinates, potential optimized DVR can further reduce the numerical costs.[160] For details of discretization, the reader is referred to excellent reviews.[159, 161]

5.2. Propagation and Product Projection

In quantum dynamical studies of molecular photodissociation, the photoexcitation is simulated by a vertical transition with proper selection rules dictated by the transition dipole.[162] The resulting initial wave packet on the excited state is then propagated with the excited state Hamiltonian. The propagation can be carried out with either the time ($e^{-i\hat{H}t}$)[161] or Chebyshev propagator ($T_k(\hat{H}) = \cos(k \arccos \hat{H})$):[163, 164]

$$\psi(t) = e^{-i\hat{H}t}\psi_0, \tag{5.7a}$$

$$\psi_{k+1} = 2\hat{H}\psi_k - \psi_{k-1} \text{ for } k>1, \qquad \psi_1 = \hat{H}\psi_0, \tag{5.7b}$$

where ψ_0 is the initial wave packet. We note that the time propagator can be interpolated by the Chebyshev propagator:[165]

$$e^{-iHt} = \sum_{k=0}^{\infty}(2-\delta_{k0})e^{-iH^{+}t}(-i)^k J_k(H^{-}t)T_k(\hat{H}_{\text{norm}}), \tag{5.8}$$

where J_k is the Bessel function of the first kind. The Hamiltonian in the Chebyshev propagation (and in Eq. (5.7b)) needs to be scaled to the spectral range of (-1,1) via, in which the spectral medium ($H^{+} = (H_{\max} + H_{\min})/2$) and half width $H^{-} = (H_{\max} - H_{\min})/2$) were determined by the spectral extrema, $H_{\max}$ and $H_{\min}$, which can be readily estimated. The Chebyshev propagator has the advantage that the propagaiton is exact and requires no interpolation such as Eq. (5.8).[166] As a result, it can be quite useful in extracting spectral infomration such as the position and width of a resonance.[163, 167] We further note that outgoing boundary conditions are often imposed by damping functions located at the edge of the radial grads to avoid reflections.

The absorption spectrum can be obtained from either the exponential Fourier transform[168] or discrete cosine Fourier transform of the respective autocorrelation function:[169]

$$\sigma(E) = \frac{4\pi\nu}{c}\text{Re}\left(\int_0^{+\infty} e^{iEt/\hbar}\langle\psi(0)|\psi(t)\rangle dt\right), \tag{5.9a}$$

$$\sigma(E) = \frac{4\pi\nu}{c}\frac{1}{H^{-}\sin\vartheta}\sum_{k=0}(2-\delta_{k,0})\cos(k\vartheta)\langle\psi_k|\psi_0\rangle, \tag{5.9b}$$

where ν is the photon frquency and c is the speed of light. The Chebyshev angle is related to the Hamiltonian ($\vartheta = \arccos E$).

Once the wave packet enters the product channel, distributions of the product ro-vibrational states can be obtained from[170]

$$A_f(E) = \left| \frac{1}{2\pi} \int_0^{+\infty} e^{iEt} C^f(t) dt \right|^2, \tag{5.10a}$$

$$A_f(E) = \left| \frac{1}{2\pi H^- \sin\vartheta} \sum_{k=0}^{N} (2 - \delta_{k0}) e^{-ik\vartheta} C_k^f \right|^2, \tag{5.10b}$$

in which $C^f(t)$ and C_k^f are the corresponding time and Chebyshev cross-correlation functions, respectively:

$$C^f(t) = \left\langle \varphi_f \delta(R - R^\infty) \middle| \psi(t) \right\rangle, \tag{5.11a}$$

$$C_k^f = \left\langle \varphi_f \delta(R - R^\infty) \middle| \psi_k \right\rangle, \tag{5.11b}$$

where φ_f denote the ro-vibrational states of the product, and R^∞ is a large value of product separation corresponding to the product channel. Similar projection methods exist for bimolecular scattering processes.[133, 164]

6. Nonadiabatic Dynamics in Photodissociation and Collisions

6.1. Photodissociation of Ammonia and Methylamine

The photodissociation of ammonia (NH_3) in its first absorption band, $NH_3 + h\nu \rightarrow NH_2(\tilde{X}^2B_1)/NH_2(\tilde{A}^2A_1) + H$, has become a prototype in understanding nonadiabatic dynamics. The electronic excitation of $NH_3(\tilde{X}^2A_1)$, which has a pyramidal shape, to planar $NH_3(\tilde{A}^2A_2)$ leads to a strong progression of the umbrella mode (ν_2) in the absorption spectrum.[171] The two electronic states form a symmetry-allowed CI at the D_{3h} configuration,[172, 173] which facilitates the nonadiabatic dissociation to the $NH_2(\tilde{X}^2B_1) + H$ products, in addition to the adiabatic dissociation to the $NH_2(\tilde{A}^2A_1) + H$ products. Truhlar and coworkers reported the first full-dimensional DPEM

for this system,[174, 175] which allowed a qualitative reproduction of experimental results.[137, 176] The full-dimensional DPEM developed later by Zhu and Yarkony[138] based on the SAP-FaD strategy[103, 104, 115] greatly improved the agreement with experiment, quantitatively reproduced the absorption spectra for both NH_3 and ND_3 and the product state distribution of $NH_2(\tilde{X}^2B_1)$.[136, 138, 139] Most importantly, the full-dimensional quantum dynamical calculations revealed that the belief of vibrationally mediated control of nonadiabatic branching in this system[177] is unsubstantiated.[178] The slow H atoms observed in the stretching-mediated photodissociation of NH_3 are attributable to the highly internally excited $NH_2(\tilde{X}^2B_1)$, rather than $NH_2(\tilde{A}^2A_1)$.[178] This reinterpretation of the experimental observations,[177] which advances our understanding of the coupling between nuclear dynamics and electronic transitions, is made possible largely by the accuracy of the DPEM and our ability to treat this problem quantum mechanically in full dimensionality.

While IC leading to the radical channel (NH_2 + H) is well understood, there has been no dynamical study to the minor molecular channel (NH + H_2). We have recently developed a NN DPEM that not only include the two lowest-lying singlet states ($1,2^2A$), but also the lowest triplet state (1^3A),[126] which allows the study of both IC and ISC, which could potentially be involved in the formation of the molecular products. The diabatization has also been used to construct property surfaces in the diabatic representation. As shown in Figure 1, the *x*-component of the ground state permanent dipole is shown in both adiabatic and diabatic representations, and the latter is smooth and amenable to fitting, as the diabatic PESs shown in the same figure.

In addition, two DPEMs for methylamine (NH_2CH_3) have recently been developed with its full fifteen dimensions.[126, 179] Preliminary quantum dynamics based on the global DPEM of Wang *et al*.[126] using a 9-dimensional model reproduced the main features of the absorption spectrum. The photodissociation dynamics, which is expected to be quite challenging due to multiple

dissociation channels, requires a quantum treatment in order to understand some peculiar quantum features observed in experiment.[180]

6.2. Photodissociation of Hydroxymethyl

The photochemistry of hydroxymethyl (CH_2OH) is more complex than that of ammonia in that several closely spaced absorption bands exist and the dissociation leads to multiple channels: $CH_2OH + h\nu \rightarrow H_2CO + H/CHOH + H$. In the lowest absorption band, which is largely structureless,[181] a CI exists between the ground (1^2A) and first excited ($2^2A(3s)$) states of CH_2OH,[182, 183] which leads to almost exclusively to the $H_2CO + H$ product channel.[184] Experimental studies of the dissociation dynamics found a clear progression in the H kinetic energy distribution, which corresponds to certain internal excitation of the co-fragment $CH_2O(\tilde{X}^1A_1)$.[184] However, the identity of the vibrational mode involved was difficult to assign. To gain insight into the nonadiabatic dissociation dynamics, a full-dimensional multi-state DPEM was constructed using the SAP-FaD method.[185] Using this DPEM, 4D and 5D quantum dynamical models with the KEO discussed in Sec. 5 were then used in search of the active vibrational model involved in the dissociation.[154, 155] These dynamical models clearly identified the C-O stretching as the excited mode in the $CH_2O(\tilde{X}^1A_1)$ product, convoluted by significant rotational excitation, responsible for the experimentally observed progression. In Figure 2, the H atom kinetic energy distribution is given at four photon wavelengths, which agree quite well with experimental data. In addition, both direct and indirect dissociation mechanisms are observed, and they lead to distinct product state distributions, which are also visible in the experimental data. Although a higher-dimensional model was successful in reproducing the absorption spectrum of the higher $3^2A(3p_x)$ state,[186] its dissociation dynamics into the two product channels remains a challenge due to difficulties associated with the complex CI seams that involve almost all coordinates.

We note in passing that a CI can also impact the dynamics at significantly lower energies through quantum interference alluded above. In the unimolecular decay of CH_2OH on its ground electronic state, the inclusion of the GP around a CI with the first excited state was shown to impact the product state distribution in a significant way.[187]

6.3. Photodissociation of Phenol

Despite of the large size of the molecule, the first absorption band has a relatively simple structure, consisting of tunneling facilitated resonances.[188] These metastable states eventually dissociate into phenoxyl by cleaving the OH bond: $C_6H_5OH + h\nu \rightarrow C_6H_5O + H$.[19] Interestingly, these predissociative states are strongly influenced by a CI between the S_1 and S_2 states much higher in energy.[189] Several DPEMs have been reported with all 33 DOFs,[54, 108, 115, 190-192] some with proper permutation symmetry, which represented a major advance in constructing high-dimensional multistate PESs. While full-dimensional quantum dynamics is still out of reach, RD models have proven effective in uncovering key insights in the nonadiabatic dissociation dynamics. Indeed, such RD quantum models revealed the S_1-S_2 CI exerts a significant impact on the tunneling dynamics in the adiabatic representation,[152, 193] via the geometric phase (GP) effect.[194-196] The GP manifests as quantum interference between two adiabatic tunneling pathways on the opposite sides of the CI. When the initial state on S_1 has no node in the out-of-plane DOF, the interference exhibits a destructive interference pattern,[197] greatly retarding the tunneling rate relative to the adiabatic model. When the initial state has already a node, the interference becomes constructive, leading to an enhancement in tunneling rate.[198] As a result, such nonadiabatic tunneling behaves very differently from its adiabatic counterpart, thanks to the tacit participation of the excited adiabat through the CI. The agreement with experiment is only possible when the GP effect is included. Similar GP effects have been found in photodissociation of other systems.[187]

The GP effect also impacts the dissociation dynamics and the product state distribution. The H kinetic energy distribution measured in photodissociation of phenol clearly showed a progression with peaks separated by about 300-500 cm^{-1}, suggesting internal excitation of the $C_6H_5O(\tilde{X}^2B_1)$ fragment .[19, 199, 200] Ashfold *et al*. assigned the progression to the ν_{16a} mode, which has a'' symmetry, because the presence of GP around the S_1-S_2 CI confines the dynamics to vibrational modes that are antisymmetric in the out-of-plane coordinate.[201] Using the DPEM of Zhu and Yarkony,[108] we argued in a recent RD quantum dynamical study that this assignment is flawed.[153] When the rotational motion of the phenoxyl fragment is included, the aforementioned restriction no longer holds. This is because it is the total nuclear (rotational + vibrational) wavefunction, rather than the vibrational wavefunction alone, that is required to have the a'' symmetry. An a'' nuclear wavefunction can be made of an a'' vibrational wavefunction and an a' rotational wavefunction ($a''_{vib} \otimes a'_{rot}$) or alternatively of an a' vibrational wavefunction and an a'' rotational wavefunction ($a'_{vib} \otimes a''_{rot}$). This is clearly shown in Figure 3, where the calculated rotational state distributions of the phenoxyl product in various vibrational states of the ν_{16a} mode are displayed. It is clear from the figure that the even/odd rotational states are associated with the odd/even vibrational quantum numbers, in observation of the symmetry restrictions. The RD quantum dissociation dynamics confirmed this conclusion, and assigned the progression mainly to the ν_{18b} mode. This work demonstrated again that a proper quantum treatment of the dynamics in the relevant DOFs on a reliable DPEM is the key to gain insights into complex nonadiabatic systems such as phenol.

6.4. Photodissociation of Formaldehyde

Formaldehyde (H_2CO) is a prototypical system for spectroscopic and dynamics studies.[202, 203] The electronic excitation from the planar $\tilde{X}^1A_1$ (S_0) state to the non-planar $\tilde{A}^1A_2$ (S_1) state is only vibronically allowed. The vibronic resonances on the S_1 state are long-lived and their non-radiative decay to the S_0 state can proceed either via IC between the S_0 and S_1 states,[204, 205] or via ISC through T_1.[206] Once on S_0, the resulting highly internally excited molecule can dissociate either to the radical channel (HCO + H) or to the much lower molecular channel (H_2 + CO).[203] Although the latter has a well-defined transition state, recent work revealed that the formation of the molecular products can also take place via roaming,[207] which can be considered as frustrated dissociation to the radical channel.[208, 209] To understand roaming dynamics, it is vital to elucidate the nonadiabatic decay mechanisms.[210] This in turn requires the development of a DPEM that includes both the IC and ISC nonadiabatic pathways.

As discussed in Sec. 4, the construction of such a DPEM takes two steps. In the first step, a singlet DPEM is constructed, in which the S_0 and S_1 states coupled by derivative coupling near the CI are characterized. The second step further incorporates the T_1 state via spin-orbit coupling with the singlets in the same diabatic representation. A 2×2 DPEM for the singlet states has already been constructed using an NN-FaD approach that preserves the permutation symmetry.[122] The diabatization of the singlet states is shown to be vital in representing the spin-orbit coupling near the CI.[125] In Figure 4, the spin-orbit coupling surfaces are shown in both the adiabatic and diabatic representations near the CI. The former has drastic discontinuities which cannot possibly be represented by analytical functions. However, these discontinuities are completed removed in the diabatic representations and their fittings are relatively straightforward. The DPEM reproduces most key features quite accurately. Quantum dynamical calculations of the low-lying vibrational states on both the S_0 and S_1 states using the DPEM found excellent agreement with experimental

band origins,[211] further validating the accuracy of the DPEM. More recently, a 5×5 DPEM for the coupled S_0, S_1, and T_1 states has been successfully developed also using an NN-FaD approach.[123] The quantum calculations of low-lying vibrational levels on the three electronic states again yielded satisfactory agreement with available experimental band origins.[123] This work also provided the permanent and transition dipole surfaces for this system, which are also fit accurately using a NN approach in the diabatic representation.

The emergence of such DPEMs will allow a proper treatment of IC and ISC on an equal footing. Such quantum dynamical calculations are expected to be quite challenging because not only more states are involved, but also the phase space to be explored is vast. However, we are confident that progress is within the reach in the near future.

6.5. Quenching of OH($A^2\Sigma^+$) by H_2

The collision between the excited OH($A^2\Sigma^+$) with H_2 leads to both a non-reactive (OH($X^2\Pi$) + H_2) channel and a reactive (H_2O + H) quenching channel.[212] These nonadiabatic channels are facilitated by CIs between the excited (3^2A) state correlated to the reactants (OH($A^2\Sigma^+$) + H_2) and two lower ones (2^2A and 1^2A) correlated to the products (OH($X^2\Pi$) + H_2) in the non-reactive quenching channel. These two CIs have different types of branching space and different seams, as shown in Figure 5.[213-216] Both the nonadiabatic channels have been investigated by Lester and coworkers,[217-219] who reported a branching ratio in strong favor to the reactive channel.[217] To understand nonadiabatic dynamics, several DPEMs with two,[218, 220] three,[128, 221] and four[222] electronic states have been developed. Although several dynamical calculations have been reported,[220, 221, 223, 224] it is only recently that a full-dimensional quantum study involving all three electronic states has become possible.

Our recent full-dimensional investigation of the nonadiabatic collisional quenching of OH($A^2\Sigma^+$) by H_2 used a time-dependent wave packet method.[225] This 4×4 DPEM used in the calculations enforces the permutation symmetry between the two H atoms in H_2 using a SAP-FaD approach,[222] which is sufficient for most dynamical needs. The quantum dynamics carried out with zero total nuclear angular momentum (N_{tot}=0) resolves not only the two nonadiabatic quenching channels, but also the adiabatic in(elastic) channel on the upper adiabat. The experimentally observed OH($X^2\Pi$) ro-vibrational state distribution are well reproduced, as shown in Figure 6, validating the DPEM. However, the reactive quenching channel was predicted to have roughly the same yield as the non-reactive quenching channel. This apparent disagreement with the experimental report[217] was resolved by noting the that the original experimental model ignored the adiabatic channel. This assumption is premature as both a later experiment[226] and theory[221, 225] all pointed to a dominant adiabatic (in)elastic scattering back to the OH($A^2\Sigma^+$) + H_2 channel. Interestingly, the large adiabatic yield can be attributed to strong stereodynamics.[225] If the OH approaches H_2 with its H end, a van der Waals well on the upper adiabat results in non-reactive scattering. When OH approaches with its O hand, however, it gains access to the CIs leading to nonadiabatic transitions to lower states. Interestingly, the nonadiabatic transition is mostly via the linear CI, as opposed to the C_{2v} CI as believed before. These two entrance channels are separated by a large barrier which prevent exchange between the two orientations. The detailed quantum dynamics on an accurate DPEM was shown again to uncover valuable insights in the nonadiabatic dynamics of this prototypical bimolecular process.

7. Summary and Prospects

The recent advances discussed in this Perspective are largely driven by the development of high-fidelity multidimensional global DPEMs for small molecular systems. This is made possible by our ability perform a large number of high-level *ab initio* calculations in the relevant configuration space, and by new machine learning approaches for representing these discrete data in analytic forms. The construction of DPEMs is intrinsically more difficult than fitting single adiabatic PESs, because not only the diabatic PESs but also their off-diagonal couplings need be described in high fidelity. The high accuracy of the *ab initio* calculations and high precision of the fits manifest in excellent agreement of quantum dynamical calculations with experimental observations. The convergence of theoretical and experimental characterization of photodissociation and bimolecular collision dynamics deepens our understanding of how nonadiabaticity affects chemical processes.

The tremendous progress notwithstanding, the current state of the field is still far from mature. Although the electronic structure theory is capable of generating PESs and DPEMs with sufficient accuracy (~ 1 kcal/mol) to qualitatively understand most experimental observations, it has certainly not achieved spectroscopic accuracy (~1 cm^{-1}). In addition, it is mostly restricted to molecules made up of light atoms. The extension of reliable *ab initio* treatments to molecular systems with heavier atoms, including transition metals, remains a challenge. In addition, extensions to larger systems also require new ideas and approaches in representing the high-dimensional DPEMs. Quantum dynamics calculations are notoriously difficult for high-dimensional systems, due to the so-called "dimensionality curse", namely the exponential increase of size with the number of coordinates. RD models are effective to some extent, so new and more powerful quantum dynamics algorithms are in high demand. The MCTDH approach has certainly shown much promise and more work in that direction is highly warranted.

We certainly are in the midst of an exciting era where our knowledge on nonadiabatic dynamics is exploding. A thorough understanding of the intricate details in small prototypical systems remains highly valued. Future studies in this field are expected to develop new and more effective theoretical tools to uncover novel features in nonadiabatic dynamics.

Acknowledgements: This work was supported by the US Department of Energy (Grant No. DE-SC0015997 to HG and DRY) and by the US National Science Foundation (Grant No. CHE-1954723 to DRY). CX thanks the National Natural Science Foundation of China (Grant No. 22073073 to CX). HG is a Humboldt Research Awardee and he thanks Prof. Dr. Alec Wodtke for his hospitality during visits to Göttingen.

References

1. M. Born and R. Oppenheimer, *Ann. Phys.*, 1927, **84**, 0457.
2. W. J. Hehre, L. Radom, P. v. R. Schleyer and J. A. Pople, *Ab initio Molecular Orbital Theory*. Wiley, New York, 1986.
3. H. Eyring and M. Polanyi, *Z. Phys. Chem.*, 1931, **12**, 279.
4. C. Qu, Q. Yu and J. M. Bowman, *Annu. Rev. Phys. Chem.*, 2018, **69**, 151.
5. B. Fu and D. H. Zhang, *J. Chem. Theo. Comput.*, 2018, **14**, 2289.
6. B. Jiang, J. Li and H. Guo, *J. Phys. Chem. Lett.*, 2020, **11**, 5120.
7. H. Köppel, W. Domcke and L. S. Cederbaum, *Adv. Chem. Phys.*, 1984, **57**, 59.
8. F. Bernardi, M. Olivucci and M. A. Robb, *Chem. Soc. Rev.*, 1996, **25**, 321.
9. I. B. Bersuker, *Chem. Rev.*, 2001, **101**, 1067.
10. G. A. Worth and L. S. Cederbaum, *Annu. Rev. Phys. Chem.*, 2004, **55**, 127.
11. A. W. Jasper, S. Nangia, C. Zhu and D. G. Truhlar, *Acc. Chem. Res.*, 2006, **39**, 101.
12. T.-S. Chu, Y. Zhang and K.-L. Han, *Int. Rev. Phys. Chem.*, 2006, **25**, 201.
13. J. C. Tully, *J. Chem. Phys.*, 2012, **137**, 22A301.
14. C. M. Marian, *WIREs: Comput. Mol. Sci.*, 2012, **2**, 187.
15. M. S. Schuurman and A. Stolow, *Annu. Rev. Phys. Chem.*, 2018, **69**, 427.
16. J. Westermayr and P. Marquetand, *Chem. Rev.*, 2020.
17. R. Schinke, *Photodissociation Dynamics*. Cambridge University Press, Cambridge, 1993.
18. L. J. Butler, *Annu. Rev. Phys. Chem.*, 1998, **49**, 125.
19. M. N. R. Ashfold, B. Cronin, A. L. Devine, R. N. Dixon and M. G. D. Nix, *Science*, 2006, **312**, 1637.

20. K. Yuan, R. N. Dixon and X. Yang, *Acc. Chem. Res.*, 2011, **44**, 369.
21. B. G. Levine and T. J. Martínez, *Annu. Rev. Phys. Chem.*, 2007, **58**, 613.
22. S. Matsika and P. Krause, *Annu. Rev. Phys. Chem.*, 2011, **62**, 621.
23. W. Domcke and D. R. Yarkony, *Annu. Rev. Phys. Chem.*, 2012, **63**, 325.
24. B. K. Kendrick, *J. Phys. Chem. A*, 2003, **107**, 6739.
25. D. R. Yarkony, *Rev. Mod. Phys.*, 1996, **68**, 985.
26. D. R. Yarkony, *Chem. Rev.*, 2011, **112**, 481.
27. J. von Neumann and E. Wigner, *Physik. Z.*, 1929, **30**, 467.
28. F. London, *Z. Phys.*, 1932, **74**, 143.
29. E. Teller, *J. Phys. Chem.*, 1937, **41**, 109.
30. G. Herzberg and H. C. Longuet-Higgins, *Discuss. Faraday Soc.*, 1963, **35**, 77.
31. W. Domcke, D. R. Yarkony and H. Köppel, *Conical Intersections: Theory, Computation, and Experiment*. World Scientific: Singapore, 2011.
32. C. A. Mead, *Rev. Mod. Phys.*, 1992, **64**, 51.
33. I. G. Ryabinkin, L. Joubert-Doriol and A. F. Izmaylov, *Acc. Chem. Res.*, 2017, **50**, 1785.
34. C. Xie, C. L. Malbon, H. Guo and D. R. Yarkony, *Acc. Chem. Res.*, 2019, **52**, 501.
35. F. An, J. Chen, X. Hu, H. Guo and D. Xie, *J. Phys. Chem. Lett.*, 2020, **11**, 4768.
36. M. Baer, *Beyond Born-Oppenheimer: Electronic Nonadiabatic Coupling Terms and Conical Intersections*. Wiley, New Jersey, 2006.
37. D. R. Yarkony, C. Xie, X. Zhu, Y. Wang, C. L. Malbon and H. Guo, *Comput. Theo. Chem.*, 2019, **1152**, 41.
38. G. A. Meek and B. G. Levine, *J. Chem. Phys.*, 2016, **144**, 184109.
39. F. T. Smith, *Phys. Rev.*, 1969, **179**, 111.
40. H. Köppel, in *Conical Intersections: Electronic Structure, Dynamics and Spectroscopy*, edited by W. Domcke, D. R. Yarkony and H. Köppel World Scientific, Singapore, 2004.
41. H. Guo and D. R. Yarkony, *Phys. Chem. Chem. Phys.*, 2016, **18**, 26335.
42. C. A. Mead and D. G. Truhlar, *J. Chem. Phys.*, 1982, **77**, 6090.
43. M. Baer, *Chem. Phys. Lett.*, 1975, **35**, 112.
44. M. Ben-Nun, J. Quenneville and T. J. Martínez, *J. Phys. Chem. A*, 2000, **104**, 5161.
45. M. Ben-Nun and T. J. Martinez, *Adv. Chem. Phys.*, 2002, **121**, 439.
46. M. Richter, P. Marquetand, J. González-Vázquez, I. Sola and L. González, *J. Chem. Theo. Comput.*, 2011, **7**, 1253.
47. S. Mai, P. Marquetand and L. González, *WIREs Comput. Mol. Sci.*, 2018, **8**, e1370.
48. B. F. E. Curchod and T. J. Martínez, *Chem. Rev.*, 2018, **118**, 3305.
49. B. G. Levine, C. Ko, J. Quenneville and T. J. MartÍnez, *Mol. Phys.*, 2006, **104**, 1039.
50. N. Minezawa and M. S. Gordon, *J. Phys. Chem. A*, 2009, **113**, 12749.
51. N. Minezawa, N. De Silva, F. Zahariev and M. S. Gordon, *J. Chem. Phys.*, 2011, **134**, 054111.
52. M. Baer, *Mole. Phys.*, 1980, **40**, 1011.
53. F. W. Warner, *Foundations of Differentiable Manifolds and Lie Group*. Springer New York, 1983.
54. C. L. Malbon, X. Zhu, H. Guo and D. R. Yarkony, *J. Chem. Phys.*, 2016, **145**, 234111.
55. D. R. Yarkony, *J. Chem. Phys.*, 1996, **105**, 10456.
56. D. R. Yarkony, *J. Chem. Phys.*, 2000, **112**, 2111.
57. C. A. Mead, *Chem. Phys.*, 1980, **49**, 33.
58. R. Abrol and A. Kuppermann, *J. Chem. Phys.*, 2002, **116**, 1035.
59. D. Yuan, Y. Guan, W. Chen, H. Zhao, S. Yu, C. Luo, Y. Tan, T. Xie, X. Wang, Z. Sun, D. H. Zhang and X. Yang, *Science*, 2018, **362**, 1289.
60. C. R. Evenhuis and M. A. Collins, *J. Chem. Phys.*, 2004, **121**, 2515.
61. O. Godsi, C. R. Evenhuis and M. A. Collins, *J. Chem. Phys.*, 2006, **125**, 104105.

62. C. Evenhuis and T. J. Martínez, *J. Chem. Phys.*, 2011, **135**, 224110.
63. Z. H. Top and M. Baer, *J. Chem. Phys.*, 1977, **66**, 1363.
64. Z. Xu, M. Baer and A. J. C. Varandas, *J. Chem. Phys.*, 2000, **112**, 2746.
65. S. Ghosh, S. Mukherjee, B. Mukherjee, S. Mandal, R. Sharma, P. Chaudhury and S. Adhikari, *J. Chem. Phys.*, 2017, **147**, 074105.
66. D. R. Yarkony, *J. Phys. Chem. A*, 1998, **102**, 8073.
67. R. J. Cave and M. D. Newton, *Chem. Phys. Lett.*, 1996, **249**, 15.
68. R. J. Cave and M. D. Newton, *J. Chem. Phys.*, 1997, **106**, 9213.
69. H. J. Werner and W. Meyer, *J. Chem. Phys.*, 1981, **74**, 5802.
70. C. E. Hoyer, X. Xu, D. Ma, L. Gagliardi and D. G. Truhlar, *J. Chem. Phys.*, 2014, **141**, 114104.
71. C. E. Hoyer, K. Parker, L. Gagliardi and D. G. Truhlar, *J. Chem. Phys.*, 2016, **144**, 194101.
72. A. J. Dobbyn and P. J. Knowles, *Mole. Phys.*, 1997, **91**, 1107.
73. J. E. Subotnik, S. Yeganeh, R. J. Cave and M. A. Ratner, *J. Chem. Phys.*, 2008, **129**, 244101.
74. X. Zhu and D. R. Yarkony, *J. Phys. Chem. A*, 2015, **119**, 12383.
75. Y. Wang and D. R. Yarkony, *J. Chem. Phys.*, 2018, **149**, 154108.
76. Y. Wang, Y. Guan and D. R. Yarkony, *J. Phys. Chem. A*, 2019, **123**, 9874.
77. S. Han, Y. Wang, Y. Guan, D. R. Yarkony and H. Guo, *J. Chem. Theo. Comput.*, 2020, **16**, 6776.
78. A. Viel and W. Eisfeld, *J. Chem. Phys.*, 2004, **120**, 4603.
79. W. Eisfeld and A. Viel, *J. Chem. Phys.*, 2005, **122**, 204317.
80. A. V. Marenich and J. E. Boggs, *Chem. Phys. Lett.*, 2005, **404**, 351.
81. D. Opalka and W. Domcke, *J. Chem. Phys.*, 2013, **138**, 224103.
82. D. Opalka and W. Domcke, *Chem. Phys. Lett.*, 2010, **494**, 134.
83. T. Lenzen and U. Manthe, *J. Chem. Phys.*, 2017, **147**, 084105.
84. D. M. G. Williams and W. Eisfeld, *J. Chem. Phys.*, 2018, **149**, 204106.
85. D. M. G. Williams and W. Eisfeld, *J. Phys. Chem. A*, 2020, **124**, 7608.
86. M. H. Alexander, *Chem. Phys.*, 1985, **92**, 337.
87. H.-J. Werner, B. Follmeg and M. H. Alexander, *J. Chem. Phys.*, 1988, **89**, 3139.
88. S. Gómez-Carrasco, A. Aguado, M. Paniagua and O. Roncero, *J. Chem. Phys.*, 2006, **125**, 164321.
89. J. C. Tully, *J. Chem. Phys.*, 1973, **58**, 1396.
90. J. C. Tully and R. K. Preston, *J. Chem. Phys.*, 1971, **55**, 562.
91. L. P. Viegas, A. Alijah and A. J. C. Varandas, *J. Phys. Chem. A*, 2005, **109**, 3307.
92. A. Aguado, O. Roncero and C. Sanz-Sanz, *Phys. Chem. Chem. Phys.*, 2021, **23**, 7735.
93. T. Pacher, L. S. Cederbaum and H. Köppel, *J. Chem. Phys.*, 1988, **89**, 7367.
94. T. Pacher, C. A. Mead, L. S. Cederbaum and H. Köppel, *J. Chem. Phys.*, 1989, **91**, 7057.
95. T. Pacher, L. S. Cederbaum and H. Köppel, *Adv. Chem. Phys.*, 1993, **84**, 293.
96. K. Ruedenberg and G. J. Atchity, *J. Chem. Phys.*, 1993, **99**, 3799.
97. G. J. Atchity and K. Ruedenberg, *Theo. Chem. Acc.*, 1997, **97**, 47.
98. N. Wittenbrink, F. Venghaus, D. Williams and W. Eisfeld, *J. Chem. Phys.*, 2016, **145**, 184108.
99. H. Nakamura and D. G. Truhlar, *J. Chem. Phys.*, 2001, **115**, 10353.
100. H. Nakamura and D. G. Truhlar, *J. Chem. Phys.*, 2002, **117**, 5576.
101. Q. Wu, L. Zhou, G. C. Schatz, Y. Zhang and H. Guo, *J. Am. Chem. Soc.*, 2020, **142**, 13090.
102. A. Thiel and H. Köppel, *J. Chem. Phys.*, 1999, **110**, 9371.
103. X. Zhu and D. R. Yarkony, *J. Chem. Phys.*, 2010, **132**, 104101.
104. X. Zhu and D. R. Yarkony, *J. Chem. Phys.*, 2012, **136**, 174110.
105. Y. Guan, H. Guo and D. R. Yarkony, *J. Chem. Phys.*, 2019, **150**, 214101.
106. D. R. Yarkony, *Acc. Chem. Res.*, 1998, **31**, 511.
107. P. R. Bunker and P. Jensen, *Molecular Symmetry and Spectroscopy*. NRC Research Press, Ottawa, 1998.

108. X. Zhu and D. R. Yarkony, *J. Chem. Phys.*, 2016, **144**, 024105.
109. B. J. Braams and J. M. Bowman, *Int. Rev. Phys. Chem.*, 2009, **28**, 577.
110. B. Fu, X. Shan, D. H. Zhang and D. C. Clary, *Chem. Soc. Rev.*, 2017, **46**, 7625.
111. J. Li, B. Zhao, D. Xie and H. Guo, *J. Phys. Chem. Lett.*, 2020, **11**, 8844.
112. B. Jiang, D. Xie and H. Guo, *J. Chem. Phys.*, 2011, **134**, 231103.
113. S. A. Ndengué, R. Dawes and H. Guo, *J. Chem. Phys.*, 2016, **144**, 244301.
114. A. J. C. Varandas, F. B. Brown, C. A. Mead, D. G. Truhlar and N. C. Blais, *J. Chem. Phys.*, 1987, **86**, 6258.
115. X. Zhu and D. R. Yarkony, *J. Chem. Phys.*, 2014, **140**, 024112
116. C. Xie, X. Zhu, D. R. Yarkony and H. Guo, *J. Chem. Phys.*, 2018, **149**, 144107.
117. S. Haykin, *Neural Networks and Learning Machines: A Comprehensive Foundation*. Prentice Hall,, Upper Saddle River, 2009.
118. B. Jiang and H. Guo, *J. Chem. Phys.*, 2013, **139**, 054112.
119. J. Li, B. Jiang and H. Guo, *J. Chem. Phys.*, 2013, **139**, 204103.
120. K. Shao, J. Chen, Z. Zhao and D. H. Zhang, *J. Chem. Phys.*, 2016, **145**, 071101.
121. B. Jiang, J. Li and H. Guo, *Int. Rev. Phys. Chem.*, 2016, **35**, 479.
122. Y. Guan, C. Xie, H. Guo and D. R. Yarkony, *J. Phys. Chem. A*, 2020, **124**, 10132.
123. Y. Guan, C. Xie, H. Guo and D. R. Yarkony, *J. Chem. Theo. Comput.*, 2021, **17**, 4157.
124. J. Behler, *Angew. Chem. Int. Ed.*, 2017, **56**, 12828.
125. Y. Guan and D. R. Yarkony, *J. Phys. Chem. Lett.*, 2020, **11**, 1848.
126. Y. Wang, Y. Guan, H. Guo and D. R. Yarkony, *J. Chem. Phys.*, 2021, **154**, 094121.
127. Y. Guan, H. Guo and D. R. Yarkony, *J. Chem. Theo. Comput.*, 2020, **16**, 302.
128. Y. Shu, J. Kryven, A. G. Sampaio de Oliveira-Filho, L. Zhang, G.-L. Song, S. L. Li, R. Meana-Pañeda, B. Fu, J. M. Bowman and D. G. Truhlar, *J. Chem. Phys.*, 2019, **151**, 104311.
129. C. E. Rasmussen and C. K. I. Williams, *Gaussian Processes for Machine Learning*. The MIT Press, Cambridge, MA, 2006.
130. G. Nyman and H.-G. Yu, *Rep. Prog. Phys.*, 2000, **63**, 1001.
131. S. C. Althorpe and D. C. Clary, *Annu. Rev. Phys. Chem.*, 2003, **54**, 493.
132. D. H. Zhang and H. Guo, *Annu. Rev. Phys. Chem.*, 2016, **67**, 135.
133. B. Zhao and H. Guo, *WIRES: Comput. Mol. Sci.*, 2017, **7**, e1301.
134. J. Tennyson and B. T. Sutcliffe, *J. Chem. Phys.*, 1982, **77**, 4061.
135. H.-G. Yu and J. T. Muckerman, *J. Mol. Spectrosc.*, 2002, **214**, 11.
136. C. Xie, J. Ma, X. Zhu, D. H. Zhang, D. R. Yarkony, D. Xie and H. Guo, *J. Phys. Chem. Lett.*, 2014, **5**, 1055.
137. W. Lai, S. Y. Lin, D. Xie and H. Guo, *J. Chem. Phys.*, 2008, **129**, 154311.
138. X. Zhu, J. Ma, D. R. Yarkony and H. Guo, *J. Chem. Phys.*, 2012, **136**, 234301.
139. J. Ma, X. Zhu, H. Guo and D. R. Yarkony, *J. Chem. Phys.*, 2012, **137**, 22A541.
140. H.-G. Yu and J. T. Muckerman, *J. Chem. Phys.*, 2002, **117**, 11139.
141. B. R. Johnson and W. P. Reinhardt, *J. Chem. Phys.*, 1986, **85**, 4538.
142. F. Gatti, C. Iung, M. Menou, Y. Justum, A. Nauts and X. Chapuisat, *J. Chem. Phys.*, 1998, **108**, 8804.
143. F. Gatti, C. Iung, M. Menou and X. Chapuisat, *J. Chem. Phys.*, 1998, **108**, 8821.
144. H.-D. Meyer, F. Gatti and G. A. Worth, *Multidimensional Quantum Dynamics: MCTDH Theory and Applications*. Wiley-VCH, 2009.
145. D. Peláez and H.-D. Meyer, *J. Chem. Phys.*, 2013, **138**, 014108.
146. M. Schröder and H.-D. Meyer, *J. Chem. Phys.*, 2017, **147**, 064105.
147. G. A. Worth, M. A. Robb and I. Burghardt, *Faraday Disc.*, 2004, **127**, 307.
148. G. W. Richings, I. Polyak, K. E. Spinlove, G. A. Worth, I. Burghardt and B. Lasorne, *Int. Rev. Phys. Chem.*, 2015, **34**, 269.

149. A. R. Menzeleev, F. Bell and T. F. Miller III, *J. Chem. Phys.*, 2014, **140**, 064103.
150. D. Bossion, S. N. Chowdhury and P. Huo, *J. Chem. Phys.*, 2021, **154**, 184106.
151. Z. Lan, W. Domcke, V. Vallet, A. L. Sobolewski and S. Mahapatra, *J. Chem. Phys.*, 2005, **122**, 224315.
152. C. Xie, J. Ma, X. Zhu, D. R. Yarkony, D. Xie and H. Guo, *J. Am. Chem. Soc.*, 2016, **138**, 7828.
153. C. Xie, B. Zhao, C. L. Malbon, D. R. Yarkony, D. Xie and H. Guo, *J. Phys. Chem. Lett.*, 2020, **11**, 191.
154. C. Xie, C. Malbon, D. R. Yarkony and H. Guo, *J. Chem. Phys.*, 2017, **146**, 224306.
155. C. Xie and H. Guo, *J. Chem. Phys.*, 2018, **148**, 044305.
156. M. H. Alexander, *J. Chem. Phys.*, 1982, **76**, 5974.
157. C. Petrongolo, *J. Chem. Phys.*, 1988, **89**, 1297.
158. R. N. Dixon, *J. Chem. Phys.*, 1995, **102**, 301.
159. J. C. Light and T. Carrington Jr., *Adv. Chem. Phys.*, 2000, **114**, 263.
160. J. Echave and D. C. Clary, *Chem. Phys. Lett.*, 1992, **190**, 225.
161. R. Kosloff, *J. Phys. Chem.*, 1988, **92**, 2087.
162. G. G. Balint-Kurti and M. Shapiro, *Chem. Phys.*, 1981, **61**, 137.
163. H. Guo, *Rev. Comput. Chem.*, 2007, **25**, 285.
164. G. G. Balint-Kurti, *Int. Rev. Phys. Chem.*, 2008, **27**, 507.
165. H. Tal-Ezer and R. Kosloff, *J. Chem. Phys.*, 1984, **81**, 3967.
166. R. Chen and H. Guo, *Comput. Phys. Commun.*, 1999, **119**, 19.
167. V. A. Mandelshtam, in *Multiparticle Quantum Scattering with Applications to Nuclear, Atomic and Molecular Physics*, edited by D. G. Truhlar and B. Simon Springer, New York, 1996, pp. 389.
168. D. Kosloff and R. Kosloff, *J. Comput. Phys.*, 1983, **52**, 35.
169. H. Guo, *J. Chem. Phys.*, 1998, **108**, 2466.
170. G. G. Balint-Kurti, R. N. Dixon and C. C. Marston, *Int. Rev. Phys. Chem.*, 1992, **11**, 317.
171. V. Vaida, W. Hess and J. L. Roebber, *J. Phys. Chem.*, 1984, **88**, 3397.
172. M. I. McCarthy, P. Rosmus, H.-J. Werner, P. Botschwina and V. Vaida, *J. Chem. Phys.*, 1987, **86**, 6693.
173. D. R. Yarkony, *J. Chem. Phys.*, 2004, **121**, 628.
174. S. Nangia and D. G. Truhlar, *J. Chem. Phys.*, 2006, **124**, 124309.
175. Z. H. Li, R. Valero and D. G. Truhlar, *Theo. Chem. Acc.*, 2007, **118**, 9.
176. W. Lai, S. Y. Lin, D. Xie and H. Guo, *J. Phys. Chem. A*, 2010, **114**, 3121.
177. F. F. Crim, *Annu. Rev. Phys. Chem.*, 1993, **44**, 397.
178. C. Xie, X. Zhu, J. Ma, D. R. Yarkony, D. Xie and H. Guo, *J. Chem. Phys.*, 2015, **142**, 091101.
179. K. A. Parker and D. G. Truhlar, *J. Chem. Phys.*, 2020, **152**, 244309.
180. M. Epshtein, A. Portnov and I. Bar, *Phys. Chem. Chem. Phys.*, 2015, **17**, 19607.
181. L. Feng, X. Huang and H. Reisler, *J. Chem. Phys.*, 2002, **117**, 4820.
182. B. C. Hoffman and D. R. Yarkony, *J. Chem. Phys.*, 2002, **116**, 8300.
183. D. R. Yarkony, *J. Chem. Phys.*, 2005, **122**, 084316.
184. C. P. Rodrigo, C. Zhou and H. Reisler, *J. Phys. Chem. A*, 2013, **117**, 12049.
185. C. L. Malbon and D. R. Yarkony, *J. Chem. Phys.*, 2017, **146**, 134302.
186. C. Xie, C. L. Malbon, D. Xie, D. R. Yarkony and H. Guo, *J. Phys. Chem. A*, 2019, **123**, 1937.
187. C. Xie, C. L. Malbon, D. R. Yarkony, D. Xie and H. Guo, *J. Am. Chem. Soc.*, 2018, **140**, 1986.
188. G. M. Roberts, A. S. Chatterley, J. D. Young and V. G. Stavros, *J. Phys. Chem. Lett.*, 2012, **3**, 348.
189. A. L. Sobolewski, W. Domcke, C. Dedonder-Lardeux and C. Jouvet, *Phys. Chem. Chem. Phys.*, 2002, **4**, 1093.
190. X. Xu, K. R. Yang and D. G. Truhlar, *J. Chem. Theo. Comput.*, 2013, **9**, 3612.
191. K. R. Yang, X. Xu, J. J. Zheng and D. G. Truhlar, *Chem. Sci.*, 2014, **5**, 4661.
192. X. Zhu, C. L. Malbon and D. R. Yarkony, *J. Chem. Phys.*, 2016, **144**, 124312.
193. C. Xie and H. Guo, *Chem. Phys. Lett.*, 2017, **683**, 222.

194. H. C. Longuet-Higgins, U. Öpik, M. H. L. Pryce and R. A. Sack, *Proc. Royal Soc. A (London)*, 1958, **244**, 1.
195. C. A. Mead, *Chem. Phys.*, 1980, **49**, 23.
196. M. V. Berry, *Proc. Royal Soc. A (London)*, 1984, **392**, 45.
197. C. Xie, D. R. Yarkony and H. Guo, *Phys. Rev. A*, 2017, **95**, 022104.
198. C. Xie, B. K. Kendrick, D. R. Yarkony and H. Guo, *J. Chem. Theo. Comput.*, 2017, **13**, 1902.
199. M. G. D. Nix, A. L. Devine, B. Cronin, R. N. Dixon and M. N. R. Ashfold, *J. Chem. Phys.*, 2006, **125**, 133318.
200. M. N. R. Ashfold, A. L. Devine, R. N. Dixon, G. A. King, M. G. D. Nix and T. A. A. Oliver, *Proc. Natl. Acad. Sci. U. S. A.*, 2008, **105**, 12701.
201. M. G. D. Nix, A. L. Devine, R. N. Dixon and M. N. R. Ashfold, *Chem. Phys. Lett.*, 2008, **463**, 305.
202. D. J. Clouthier and D. A. Ramsay, *Annu. Rev. Anal. Chem.*, 1983, **34**, 31.
203. C. B. Moore and J. C. Weisshaar, *Annu. Rev. Phys. Chem.*, 1983, **34**, 525.
204. J. B. Simonsen, N. Rusteika, M. S. Johnson and T. I. Sølling, *Phys. Chem. Chem. Phys.*, 2008, **10**, 674.
205. M. Araujo, B. Lasorne, M. J. Bearpark and M. A. Robb, *J. Phys. Chem. A*, 2008, **112**, 7489.
206. P. Zhang, S. Maeda, K. Morokuma and B. J. Braams, *J. Chem. Phys.*, 2009, **130**, 114304.
207. D. Townsend, S. A. Lahankar, S. K. Lee, S. D. Chambreau, A. G. Suits, X. Zhang, J. Rheinecker, L. B. Harding and J. M. Bowman, *Science*, 2004, **306**, 1158.
208. J. M. Bowman and B. C. Shepler, *Annu. Rev. Phys. Chem.*, 2011, **62**, 531.
209. A. G. Suits, *Annu. Rev. Phys. Chem.*, 2020, **71**, 77.
210. B. Fu, B. C. Shepler and J. M. Bowman, *J. Am. Chem. Soc.*, 2011, **133**, 7957.
211. C. Xie, Y. Guan, D. R. Yarkony and H. Guo, *Mole. Phys.*, 2021, **in press**, e1918775.
212. M. W. Todd, D. T. Anderson and M. I. Lester, *J. Phys. Chem. A*, 2001, **105**, 10031.
213. D. R. Yarkony, *J. Chem. Phys.*, 1999, **111**, 6661.
214. B. C. Hoffman and D. R. Yarkony, *J. Chem. Phys.*, 2000, **113**, 10091.
215. J. Dillon and D. R. Yarkony, *J. Chem. Phys.*, 2013, **139**, 064314.
216. J. Dillon and D. R. Yarkony, *J. Phys. Chem. A*, 2013, **117**, 7344.
217. L. P. Dempsey, C. Murray and M. I. Lester, *J. Chem. Phys.*, 2007, **127**, 151101.
218. P. A. Cleary, L. P. Dempsey, C. Murray, M. I. Lester, J. Kłos and M. H. Alexander, *J. Chem. Phys.*, 2007, **126**, 204316.
219. L. P. Dempsey, C. Murray, P. A. Cleary and M. I. Lester, *Phys. Chem. Chem. Phys.*, 2008, **10**, 1424.
220. P.-Y. Zhang, R.-F. Lu, T.-S. Chu and K.-L. Han, *J. Chem. Phys.*, 2010, **133**, 174316.
221. M. A. Collins, O. Godsi, S. Liu and D. H. Zhang, *J. Chem. Phys.*, 2011, **135**, 234307.
222. C. L. Malbon, B. Zhao, H. Guo and D. R. Yarkony, *Phys. Chem. Chem. Phys.*, 2020, **22**, 13516.
223. B. Fu, E. Kamarchik and J. M. Bowman, *J. Chem. Phys.*, 2010, **133**, 164306.
224. P.-Y. Zhang, R.-F. Lu, T.-S. Chu and K.-L. Han, *J. Phys. Chem. A*, 2010, **114**, 6565.
225. B. Zhao, S. Han, C. L. Malbon, U. Manthe, D. R. Yarkony and H. Guo, *Nat. Chem.*, 2021, **in press**.
226. M. Brouard, J. Lawlor, G. McCrudden, T. Perkins, S. A. Seamons, P. Stevenson, H. Chadwick and F. J. Aoiz, *J. Chem. Phys.*, 2017, **146**, 244313.

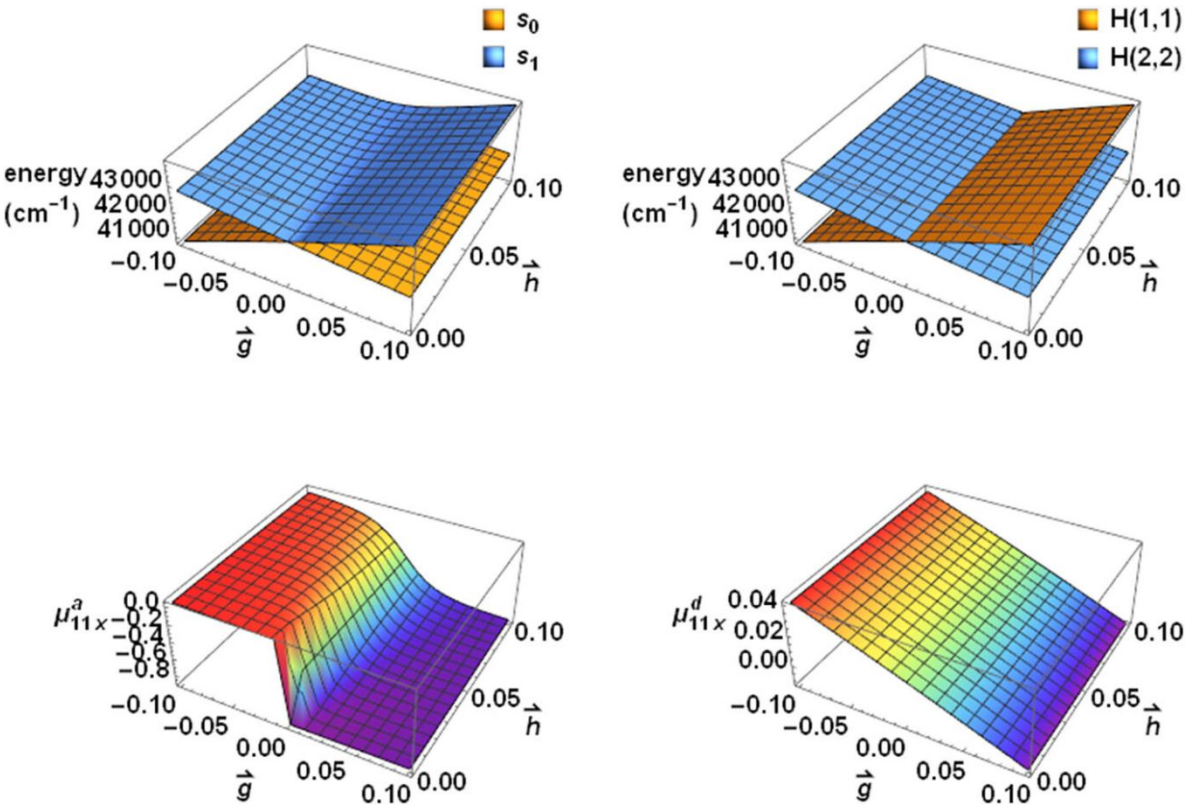

Figure 1. Upper panel: potential energy surfaces of NH_3 in both the adiabatic (S_0, S_1) and diabatic (H(1,1) and H(2,2)) representations along the **g** and **h** vectors in the vicinity of the CI. Lower panel: the x-component of the ground state permanent dipole are also shown in the two representations. Adapted with permission from Ref. [126].

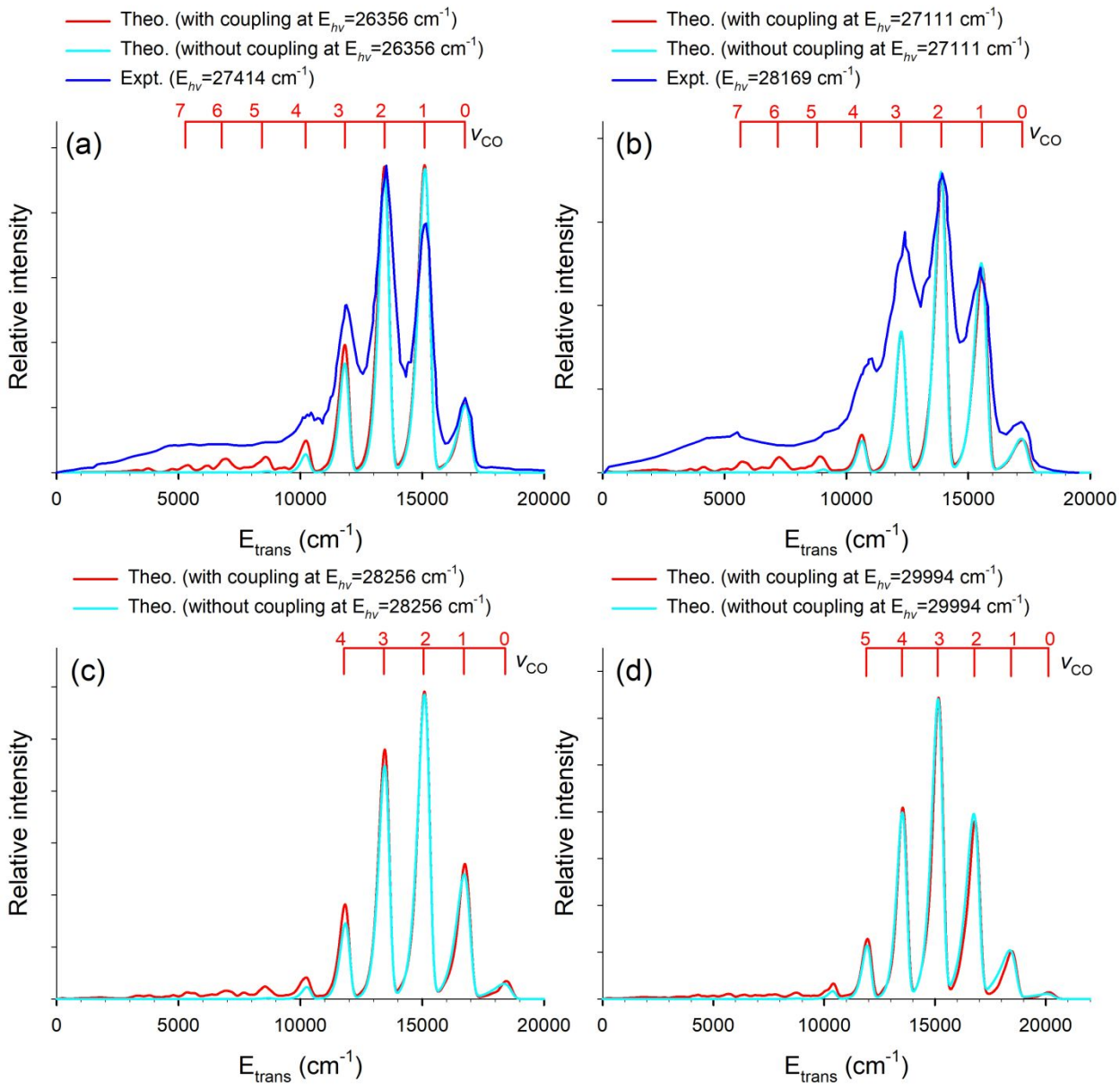

Figure 2. Calculated H atom kinetic energy distribution upon photodissociation of CH_2OH in its first excited $2^2A(3s)$ state at four photon wavelengths. The experimental distributions at two wavelengths are also given for comparison. Reproduced from Ref. [154] with permission.

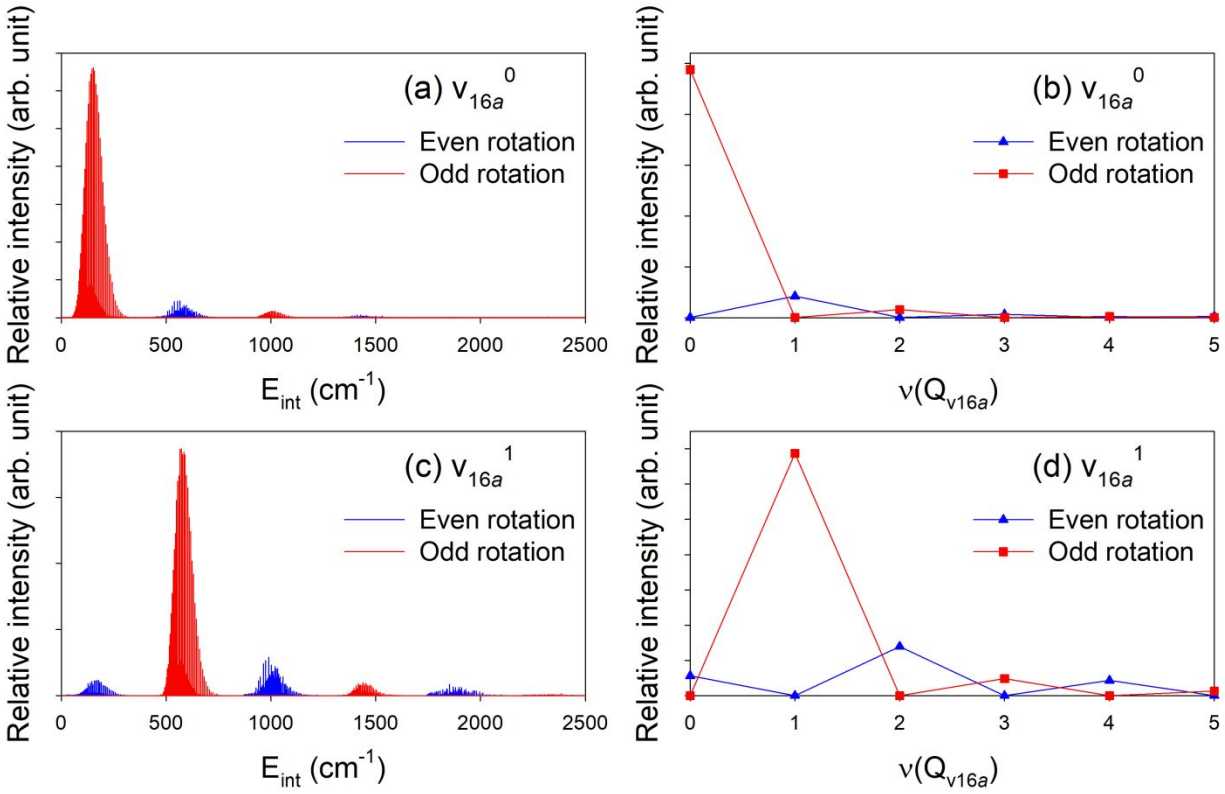

Figure 3. Phenoxyl product ro-vibrational state distributions upon photodissociation of phenol calculated using a reduced dimensional model. Even/odd rotational states are associated with the odd/even quantum numbers for the ν_{16a} mode. Reproduced with permission from Ref. [153].

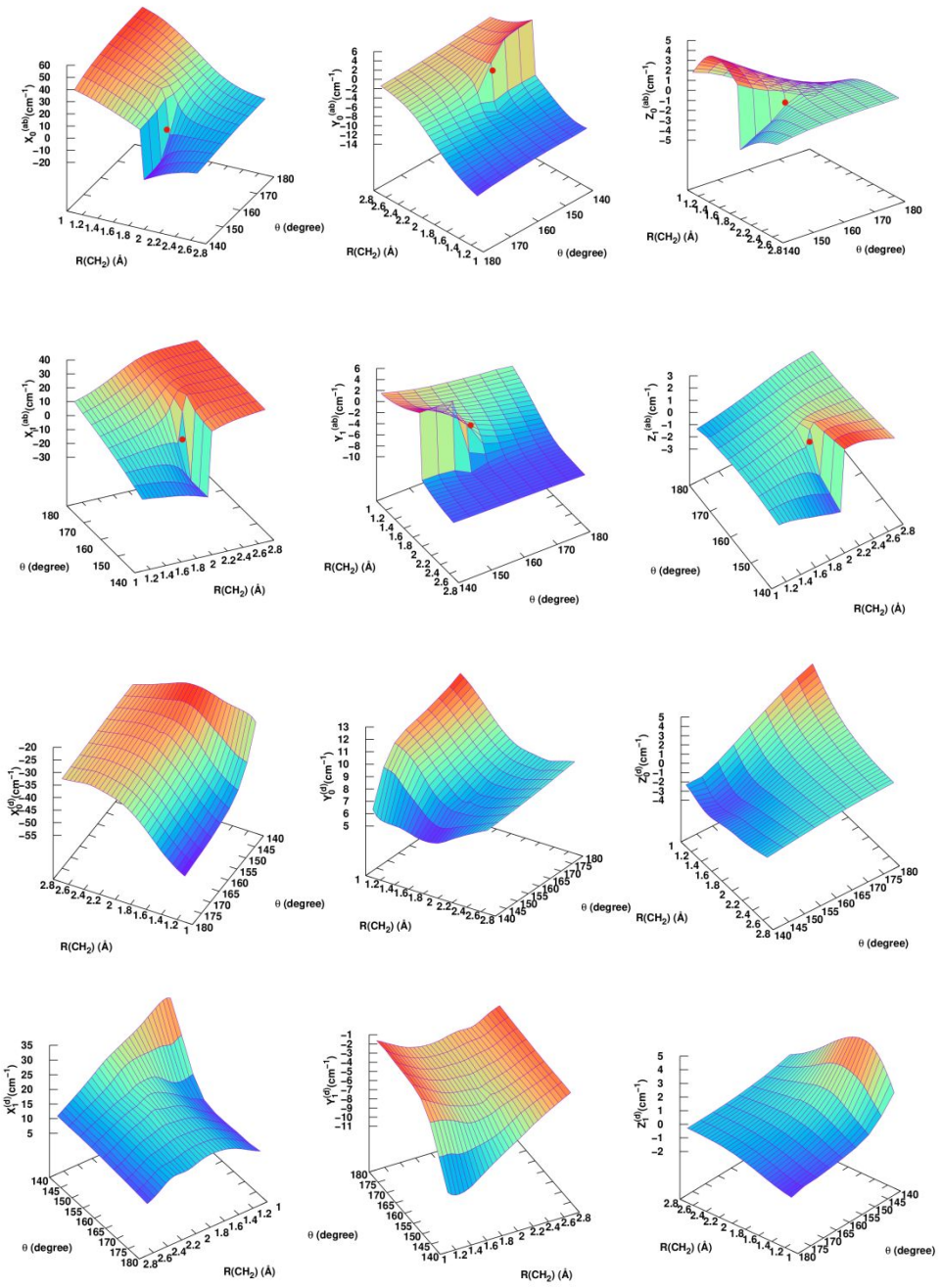

Figure 4. Spin-orbit coupling surfaces between the lowest singlet and triplet states of H_2CO in both the adiabatic (upper six panels) and diabatic (lower six panels) representation. Reproduced with permission from Ref. [127].

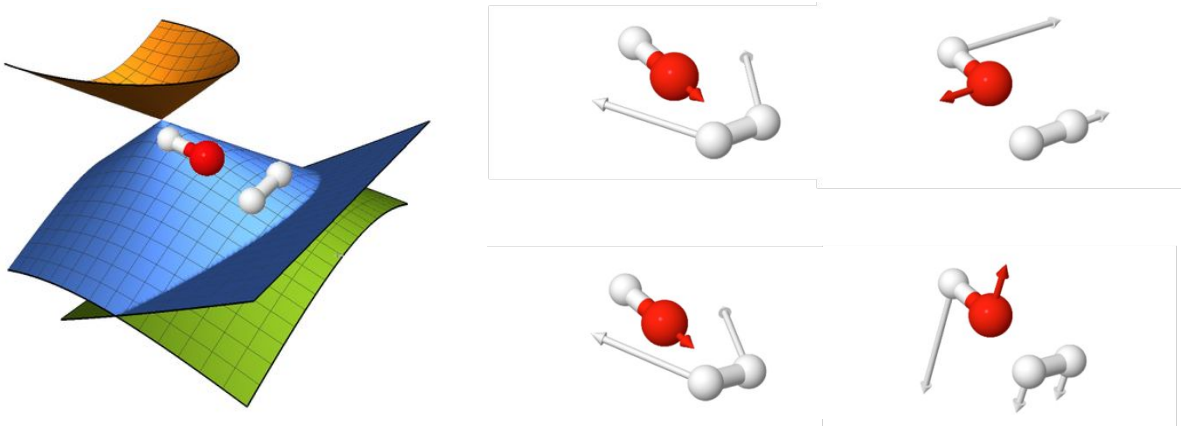

Figure 5. Adiabatic potential energy surfaces of the three lowest lying electronic states of the H_3O system near the 2^2A–3^2A C_{2v} CIs are shown on the left. x and y represent coordinates in the **g**–**h** plane (in atomic units). The mass weighted **g** and **h** vectors for the 2^2A–3^2A and 1^2A–3^2A CIs are shown on the right. Reproduced with permission from Ref. [222].

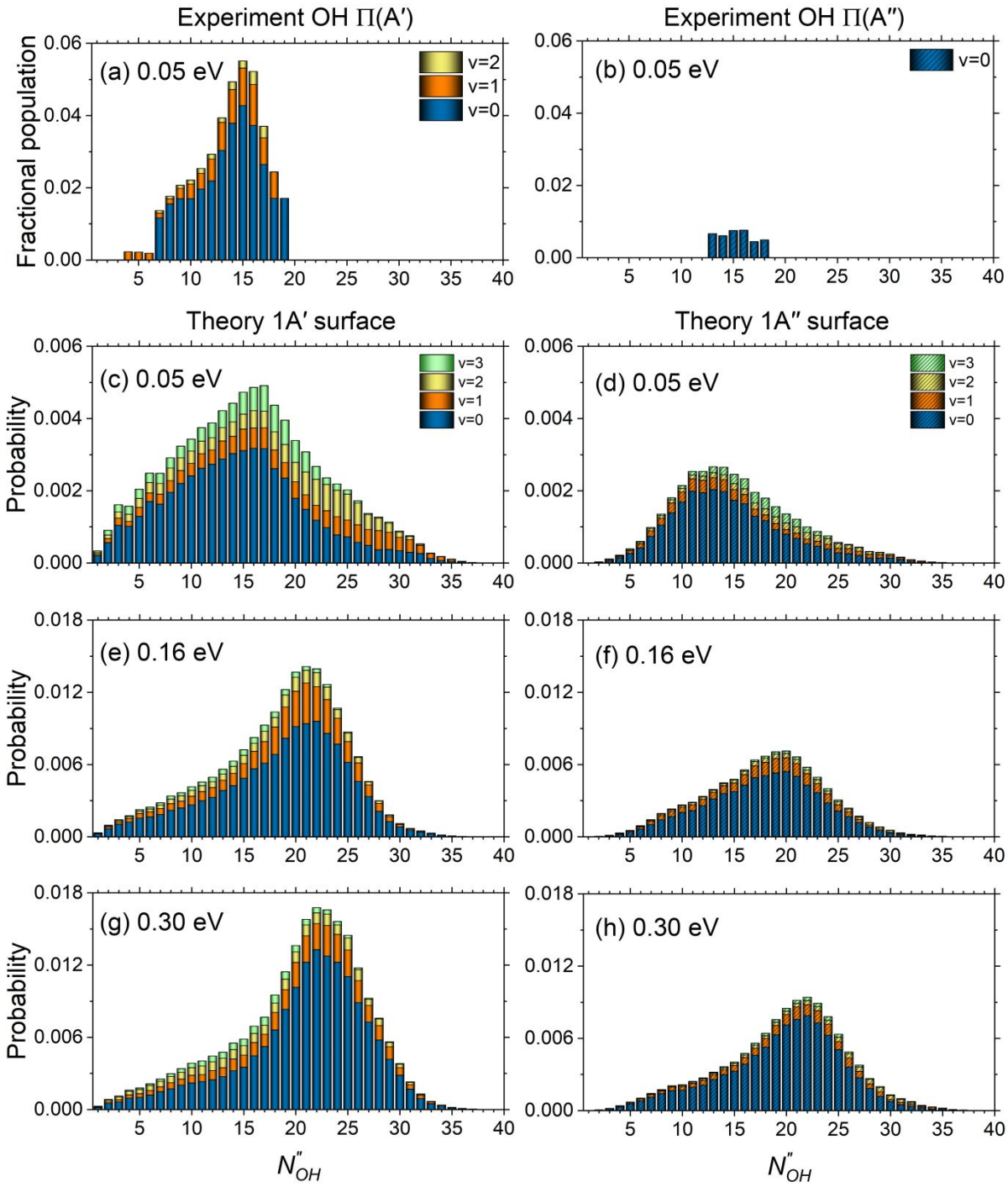

Figure 6. Calculated ro-vibrational state distributions of the OH(X) product in the H_2 quenching of OH(A) calculated using a full dimensional quantum model. The experimental distributions are shown in the top panel for comparison. Reproduced with permission from Ref. [225].